Geoderma 271 (2016) 99–114

Contents lists available at ScienceDirect

Geoderma

journal homepage: www.elsevier.com/locate/geoderma

# Chemical and textural controls on the formation of sepiolite, palygorskite and dolomite in volcanic soils

Javier Cuadros [a,*], Jose L. Diaz-Hernandez [b], Antonio Sanchez-Navas [c], Antonio Garcia-Casco [c], Jorge Yepes [d]

[a] Department of Earth Sciences, Natural History Museum, Cromwell Road, London SW7 5BD, United Kingdom
[b] IFAPA, Área de Recursos Naturales, Consejería de Agricultura, Pesca y Medio Ambiente, Junta de Andalucía, 18080 Granada, Spain
[c] Departamento de Mineralogía y Petrología—IACT, Universidad de Granada—CISC, 18071 Granada, Spain
[d] Departamento de Ingeniería Civil, IOCAG, Universidad de las Palmas de Gran Canaria, 35017 Las Palmas de GC, Spain

ARTICLE INFO

*Article history:*
Received 4 September 2015
Received in revised form 4 December 2015
Accepted 31 January 2016
Available online xxxx

*Keywords:*
Calcite
Dolomite
Palygorskite
Sepiolite
Tephra alteration
Volcanic soils

ABSTRACT

A 3-m deep soil profile from Gran Canaria, Canary Islands, has been studied. The profile is interesting because soil development on mafic tephra produced a pattern of clay mineral and carbonate distribution. Carbonates precipitated abundantly, increasingly towards the bottom, making up 20–90 wt.% of the soil. Sepiolite and calcite are dominant at the top, whereas palygorskite and dolomite are the major components at the lower part of the profile. Quartz is present in low amounts in most of the profile, and smectite and non-crystalline partially altered tephra occur in low amounts towards the bottom. Mineralogical, chemical and textural investigations indicate that sepiolite and calcite precipitated in the space between the original tephra grains, from Ca, Mg and Si dissolved in situ and transported in the runoff. Palygorskite and smectite precipitated within tephra grains, from in situ tephra weathering, as well as dolomite. The distribution of the clay minerals is due to clay composition and ion mobility. Sepiolite, consisting only of Si and Mg, precipitated outside tephra grains, where the mobile Si and Mg ions were abundant in the interstitial waters. Palygorskite and smectite contain Si, Al, Fe, and Mg and only precipitated within the tephra grains, where the immobile Al and Fe were available. Calcite precipitation in solution is kinetically favored over that of dolomite and thus calcite precipitated between the grains. Dolomite precipitated within altering tephra grains and spherical clay structures because tephra and clay generated a viscous medium where dolomite supersaturation increased and the kinetic barrier for precipitation was overcome. These results are relevant to the "dolomite problem", as they illustrate how dolomite can precipitate in surface conditions, and to $CO_2$ sequestration, because dolomite can immobilize higher $CO_2$ amounts (both Ca and Mg are involved and not only Ca) and in a much more stable manner (dolomite is eight orders of magnitude less soluble than calcite).

## 1. Introduction

Chemical weathering of basaltic volcaniclastic rocks leads to the formation of diverse clay mineral assemblages depending on the depositional environment (lacustrine, soils, alluvial terraces and marine fan deltas). Pedogenic alteration constitutes a sub-aerial weathering process involving the combined effect of diverse factors, such as parent material, climate, biota, time and geomorphology. Weathering of a basaltic substrate produces as secondary minerals clays, carbonates, zeolites and Si–Al–Fe oxy-hydroxides (Chamley, 1989). The main clay minerals derived from pedogenically-altered basaltic substrates are smectite (nontronite, saponite or montmorillonite), kaolinite and halloysite (Chamley, 1989). Sepiolite and palygorskite occur in soils derived from several substrates, in particular they are typical of caliches formed in arid and semi-arid areas (Neaman and Singer, 2004). Sub-aerial weathering by meteoric waters of basaltic substrates can provide Si–Mg bearing solutions and suitable physico-chemical conditions (mostly high pH) to precipitate Mg-rich phyllosilicates and carbonates (Singer and Norrish, 1974). Sepiolite and palygorskite are among the most Mg-rich clay minerals (Singer, 2002). Sepiolite contains more Mg than palygorskite and may derive from Mg-leaching reactions affecting palygorskite (Corma et al., 1987; Corma et al., 1990; Singer, 1977).

Altered basalts may constitute geological formations for natural $CO_2$ storage (Oelkers et al., 2008). Particularly, in pedogenic environments, $CO_2$-rich fluids produce the leaching of metals from the basaltic substrate and, under arid conditions, lead to the formation of Ca and Mg carbonates. Although some authors have identified dolomite in soils (e.g., Gile, 1961; St. Arnaud, 1979; Sobecki and Karathanasis, 1987; Botha and Hughes, 1992), there are few reports showing its pedogenic origin. Dolomite pedogeneis has been usually interpreted to take place in saline soils (Shermann et al., 1962; Kohut et al., 1995) and in soils developed on serpentinites and basaltic rocks (Podwojewski, 1995; Capo

---

* Corresponding author.
*E-mail address:* j.cuadros@nhm.ac.uk (J. Cuadros).

http://dx.doi.org/10.1016/j.geoderma.2016.01.042
0016-7061/

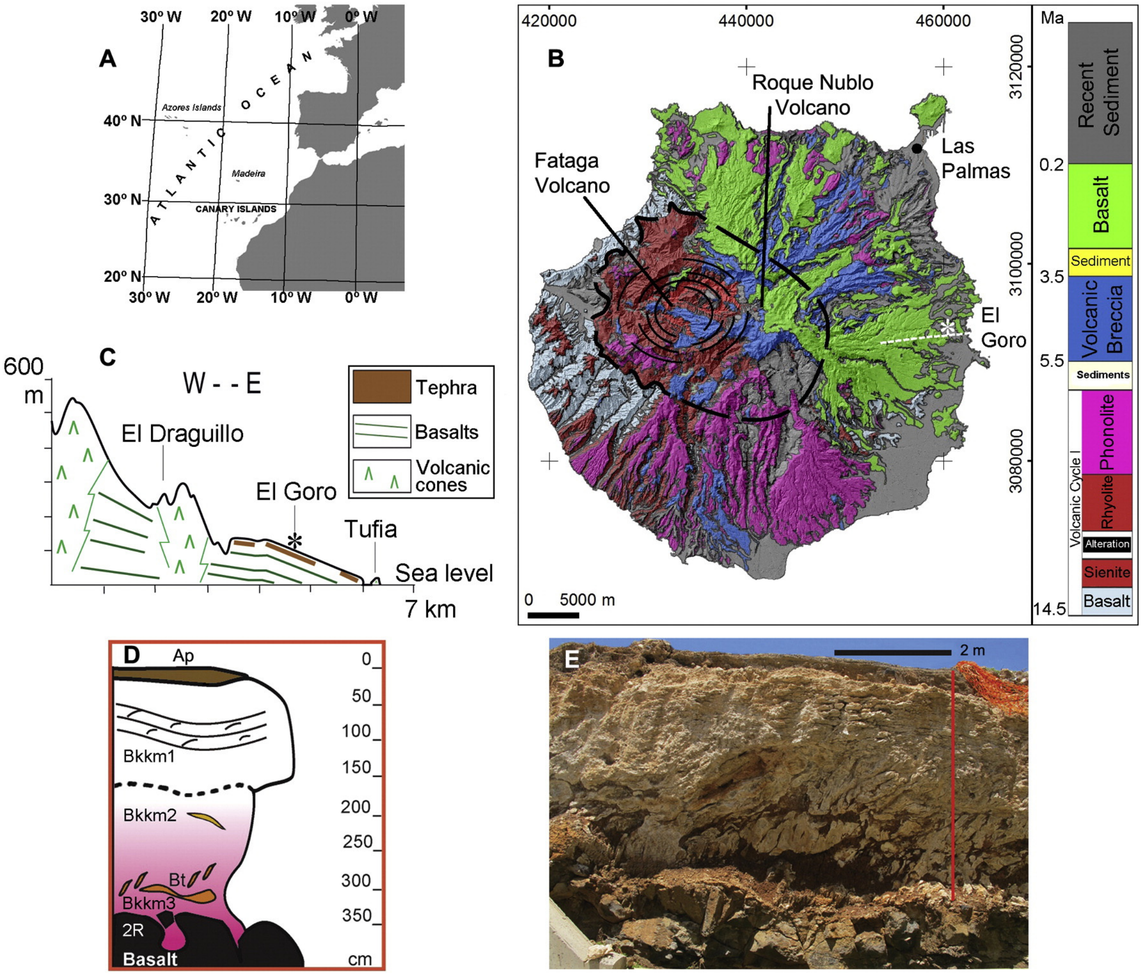

**Fig. 1.** A) Situation of the Canary Islands. B) Geological chart and lithological column of the Gran Canaria Island with indication of the diverse volcanic episodes which formed the island. The studied profile at El Goro (star) developed from tephra deposited on the eastern slopes of the Roque Nublo volcano. C) Cross section indicated in B, showing the spatial relationship between the volcanic cones (e.g., El Draguillo, of the same unit as the tephra where the soil developed), and the deposits of lavas and tephra. D) Sketch and field image (E) of the soil profile with the established horizons: Ap, Bkkm1, Bkkm2 including Bt, and Bkkm3. The basaltic substrate appears at the bottom. The sampled profile is indicated by a vertical line in E.

et al., 2000) as both environments produce or can produce high Mg concentrations. The formation of dolomite in Mg-rich soils has been recently reported by Capo et al. (2000) and Diaz-Hernandez et al. (2013) on a basaltic weathering profile in Hawaii and a clay-rich sediment in southern Spain, respectively. The Mg source was the basalt in the Hawaiian soil and detrital dolomite dissolved in the surface horizons, in the Spanish soil. The scarce formation of dolomite in modern environments contrasts with its abundance in ancient rocks, which together with failure in the efforts to synthesize dolomite in the laboratory under surface abiotic conditions has generated the so-called "dolomite problem" (e.g., Arvidson and Mackenzie, 1999).

Assemblages of Mg- and Fe-bearing clays with Fe–Mg–Ca carbonates have been detected by spectral analysis of NASA's CRISM (Compact Reconnaissance Imaging Spectrometer for Mars) images in some regions of Mars with exposed rock units dating from the Noachian period (Niles et al., 2012). Thus, soils derived from basalts under arid-semiarid conditions constitute a potential Earth analogue to the Mars carbonate and phyllosilicate-bearing rock units. Although sepiolite and palygorskite have not been identified on Mars, their spectral near-infrared features can be very similar to smectite of various Al–Mg–Fe contents, and their presence in Martian rocks is possible. Basalts are also a potential habitat for microbial life (Thorseth et al., 1992) given their abundant inorganic nutrients. Clay-carbonate assemblages on Mars are appropriate targets for the search of life relicts (Michalski et al., 2013) and the study of the bio-geochemical characteristics of Mg-bearing clay-carbonate assemblages on Earth developed on basalt may help the investigation of the possible development of life on Mars during the Noachian period.

In this work we examine a case of formation of sepiolite and palygorskite together with calcite and dolomite from pedogenic alteration of basaltic tephra, in an unusually thick 3 m soil profile. The detailed mineralogical, textural and compositional study shows a mineral distribution consisting of sepiolite and calcite as the major components at the upper part of the profile, palygorskite and dolomite in the lower part, and smectite at the bottom. We discuss this mineral and chemical zoning in the context of the alteration processes taking place in the volcanic deposit and the formation of caliche soil, as well as the role of clay minerals and tephra in the formation of dolomite.

## 2. Geological setting

Gran Canaria is the third largest island of the Canary Islands volcanic archipelago, which is part of the so called Macaronesian region, and is located just off the northwest coast of Africa (Fig. 1A). The Canary Islands are located on the oceanic crust of the African continental margin. Oceanic intraplate alkaline volcanism, probably related to a volcanic plume or hot spot in the mantle, is responsible for the formation of the archipelago. Volcanism in the Gran Canaria island evolved from an old submarine-subaerial stage (14.5–8.0 My; Guillou et al., 2004) which created a large basaltic edifice (the Shield Volcano) and a salic stratovolcano (the Fataga Volcano). The latter then experienced a caldera collapse (Guillou et al., 2004). This first stage was followed by a calm

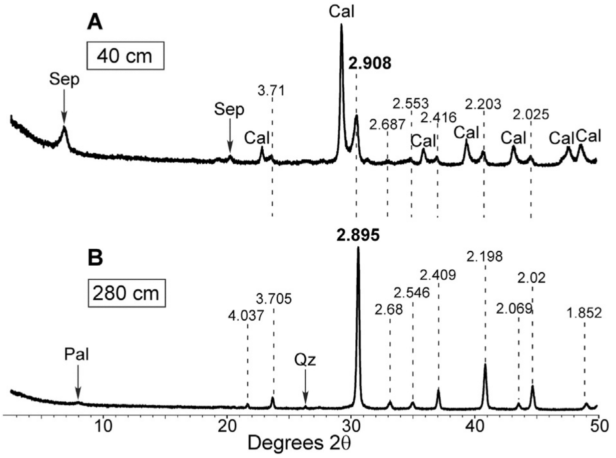

**Fig. 2.** Powder XRD diagrams of two representative whole-rock samples from 40 and 280 cm depth in the studied profile. The d-spacing values in Å of the dolomite peaks are indicated. Cal: calcite; Pal: palygorskite; Qz: quartz; Sep: sepiolite.

period (of ~3 My; Pérez-Torrado, 2000; Guillou et al., 2004) marked by erosion of the relief (drainage net incision). Then, the Roque Nublo and Post-Roque Nublo volcanic cycles (last 5.5 My; Pérez-Torrado et al., 1995; Guillou et al., 2004) took place, which formed the central stratovolcano Roque Nublo (2500 m ASL; 5.5–3.5 My; Pérez-Torrado et al., 1997; Guillou et al., 2004). The circular shape of the Gran Canaria Island is due to the large amount of salic and basic lavas and ignimbrites ejected from the central part of the island during these three stages. The Post-Roque Nublo group (~3–1.5 My: McDougall and Schmincke, 1976; Balcells et al., 1992; Guillou et al., 2004) represents the unit with the least volume of volcanic material emitted during the evolution of the subaerial volcanism of the Gran Canaria island, and only covers the north eastern part of the island (Fig. 1B). Volcanism has continued until today (809–2.9 ky: Rodríguez-González et al., 2009) but the relief has been scarcely modified by recent emissions, mainly intracanyon lava-flows.

The studied soil profile (Typic Petrocalcid, see below) is located in the lower part of fan deposits occurring in the north eastern slopes of the island, close to the El Goro village (27°57′53″N; 15°23′50″W; Fig. 1B, C). It consists of deep carbonate soils developed for hundreds of thousands to thousands of years within clastic volcanic materials (hereafter referred to as tephra) originated by the collapse of a scoria cone (Fig. 1C–E). The original scoria cone was emplaced sometime between 3 My and 3 ky before present (Guillou et al., 2004; Rodríguez-González et al., 2012). The existing tephra and related basalts in the area vary in composition from basanites to nephelinites. Their mineralogy consists of olivine, augite and nepheline phenocrysts, and low-crystallinity plagioclase in a micro-cryptocrystalline matrix (Balcells et al., 1992). Remains of fine-grained tephra included in the caliche, mainly formed by lapilli fragments, are highly vesiculated with a hipocrystalline texture. The studied carbonate soil formed from the alteration of volcanic breccia (not from the massive basaltic lavas as those observed at the bottom of the profile) of high porosity, low bulk-density and a wide range of particle size (mm to cm scale). The degree of homogeneity of the original breccia is unknown. These soils formed under prevalent arid and semiarid conditions alternating with more humid periods, as indicated by the climatic patterns proposed by Moreno et al. (2002) deduced from the study of deep-sea cores in the North Canary Basin. During the arid-semi arid periods, calcite and dolomite precipitated massively after the dissolution of Ca, Mg-rich silicate minerals of the volcanic parent material due to reaction with the $CO_2$ released in the soil by plant and microbial respiration and organic matter decay.

## 3. Material and methods

The studied profile is exposed by an artificial pit with a total depth of >3 m, located at the locality of El Goro. The present conditions correspond to a regime of aridic/torric soil moisture and hyperthermic soil temperature (Soil Survey Staff, 2014; Rodríguez et al., 2010). The profile is a complex caliche topped by a loose and anthropized surficial horizon (Ap). Using Soil Taxonomy standards (Soil Survey Staff, 2014), the caliche profile can be divided from top to bottom in three main horizons: a massive/laminar caliche (Bkkm1 horizon), a mixed horizon containing red lenses with clay (Bt) within the massive carbonates (Bkkm2), and a partially laminar caliche (Bkkm3) close to the underlying basalts (2R) (Fig. 1D, E). The boundaries between horizons can be described (Schoeneberger et al., 2012) as follows, Ap-Bkkm1 gradual and wavy; Bkkm1-Bkkm2 diffuse and wavy; Bkkm2–Bkkm3 clear and irregular; the Bt horizon is discontinuous, and the boundary is clear and irregular; Bkkm3-basalt abrupt and irregular. There are no signs of erosive surface

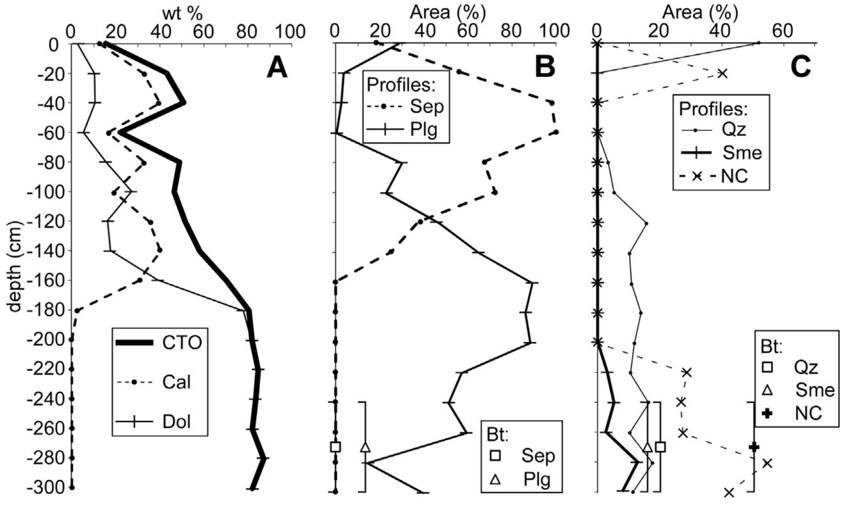

**Fig. 3.** Mineralogical variations along the studied profile. A) Weight percent content of calcite (Cal), dolomite (Dol) and total carbonates (CTO) from XRD of whole-rock samples. B) and C) Distribution profiles of sepiolite (Sep), palygorskite (Plg), smectite (Sme), quartz (Qz) and non-crystalline material (NC) assessed from powder XRD patterns of the decarbonated samples by measuring the integrated area of prominent mineral peaks (see methods for details). The areas are normalized to all phases in B and C, but two plots are used for clarity. The sample from the Bt lenses is also represented in B and C. The symbols indicate the location of the analyzed Bt sample and the brackets show the depth range in which these Bt lenses were found in the profile.

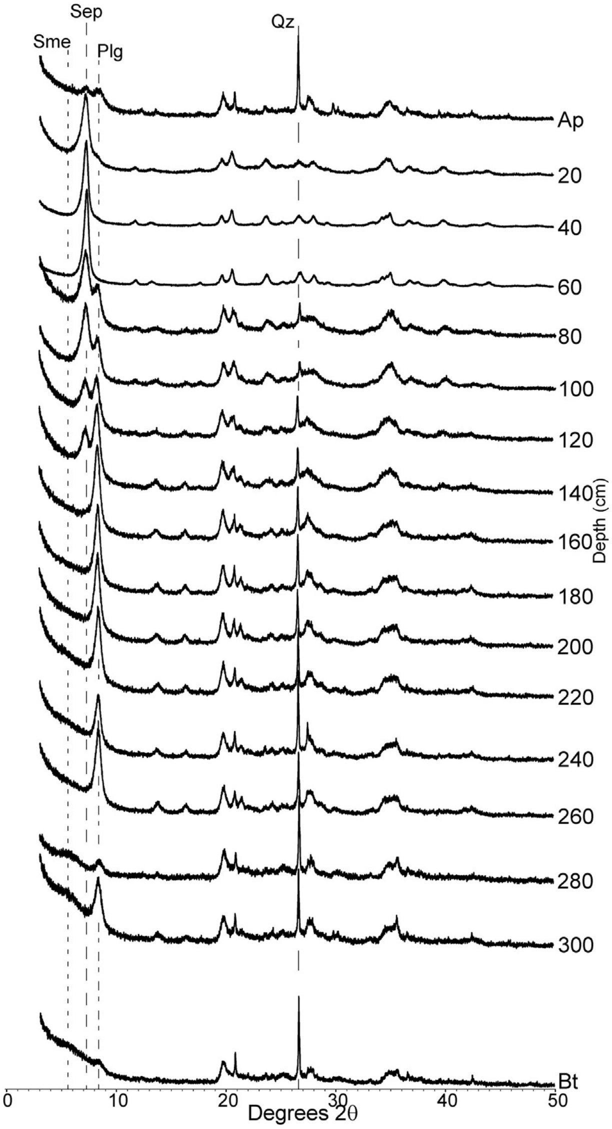

**Fig. 4.** Powder XRD patterns sequence from decarbonated samples along the profile, including one sample from the Bt lenses that did not contain carbonates. Bt lenses appear at several depths at the bottom of the sequence; the one here corresponds to ~270 cm. Plg: palygorskite; Qz: quartz; Sep: sepiolite; Sme: smectite.

or colluvial deposition and thus all the above boundaries are truly pedogenic. The morphology of the soil horizons is mostly controlled by carbonate precipitation and the consequent hardening and consolidation, rather than by the alteration of the original tephra. The soil was sampled at intervals of 20 cm from the top to the substratum. Fifteen of the studied samples correspond to carbonate-rich soil (from 20 to 300 cm deep). In addition, the basalt of the substratum (below 300 cm), the surficial horizon (sample Ap; 0–20 cm) and one sample from the reddish lenses (sample Bt; ~270 cm) located within the carbonate-rich soil, were also analyzed. The pH of the soil ranges within 7.8–8.7, with a tendency to increase from top to bottom.

Whole-rock soil samples were investigated using several techniques. First, powders obtained after grinding on a steel disk mill during 3 s, were analyzed by X-ray diffraction of the random powders by using a PANalytical X'Pert Pro diffractometer (Cu-K$\alpha$ radiation, 45 kV, 40 mA) equipped with an X'Celerator solid-state lineal detector. This detector covers an angle of 2.1° and integrates the diffracted intensity over this angle dynamically as it scans. The diffraction patterns were obtained by a continuous scan between 3 and 50 °2θ, with a 0.01 °2θ resolution, ~15 min total scan time (equivalent to 20 s counting time per 0.01 °2θ). The data were processed using the XPOWDER program (Martín-Ramos et al., 2012) for visualization of the X-ray patterns and determination of the qualitative and quantitative mineral composition of the whole-rock samples.

In the second place, pieces of the soil samples (with a rock-type consistency) at 60, 100 and 300 cm depth were consolidated using a polyester resin, prepared as polished sections and carbon coated for the textural, mineralogical and compositional study by analytical scanning electron microscopy and electron microprobe analysis. SEM back-scattered electron (BSE) images and energy-dispersion X-ray (EDX) spot analyses (200 nm of diameter) were obtained with a high-resolution field-emission scanning electron microscope (FESEM) Auriga (Carl Zeiss) equipped with a LinK INCA 200 (Oxford Instruments) analytical system. In addition, secondary electron (SE) images were also obtained to examine the micromorphology of the clay minerals and related carbonates.

Quantitative single-point analysis and X-ray element maps from the sample at 100 cm depth only were acquired with an electron microprobe CAMECA SX100 (see Garcia-Casco et al., 1993, for details of routine operation conditions). For single point analysis, the working conditions were 20 kV of acceleration voltage, 5 nA of probe current and 5 μm diameter of the spot size. For the X-ray maps, the corresponding values varied depending on the abundance of carbonates in the analyzed area because they are more easily damaged by the electron beam than silicates. Thus, for areas dominated by silicates, 15 kV, 110 nA, 1 μm step size (each step generates a pixel in the map) and 30 ms of counting time per pixel were used. We have found that a relatively high beam current (110 nA) combined with short counting time (milliseconds rather than seconds) precludes beam damage to silicates (Garcia-Casco, 2007). Where carbonates were abundant, a much lower beam current of 30 nA was used, together with 15 kV, 2 μm pixel size and 70 ms counting time per pixel. With this low beam current and short counting time carbonate damage is not expected. X-ray element maps were obtained by moving the sample relative to the electron beam.

Images were processed with the software DWImager (Torres-Roldan and Garcia-Casco, 2003) to obtain quantitative compositional data. The method of Bence and Albee (1968) was followed for matrix correction by using the composition of internal standards of silicates analyzed with the electron microprobe, the $\alpha$-factor table by Kato (2005), and a correction for 3.5 μs dead time. Colour mineral-phase maps were overlain onto a grey-scale base-layer calculated as $\Sigma\ (counts_i \cdot A_i)$, (where $A$ is atomic number and $i$ is Si, Ti, Al, Fe, Mg, Ca, Na, and K), which contains the basic textural information of the scanned areas.

The study of the silicate component of the fifteen carbonate-rich soil samples (from 20 to 300 cm) was carried out by removing carbonates by reaction of the whole-rock powders with diluted acetic acid at 60 °C and then washing the silicate residue repeatedly with distilled water. The sample from the Bt did not contain carbonates, and therefore was not attacked with acid. The sample from the Ap horizon contained allocthonous rock fragments, for which reason the fraction <2 mm was first selected by dry sieving and then decarbonated.

Major-element composition of the decarbonated samples, the basalt and the Bt sample was determined by using a wavelength-dispersive XRF sequential spectrometer S4 Pioneer (BRUKER). Lithium tetraborate fused beads were employed for bulk sample homogenization. Typical precision was better than ±1.5% for an analyte concentration of 10 wt.%. Zirconium was determined by X-ray fluorescence with a precision better than ±4% for 100 ppm Zr. REE and other trace elements were analyzed by ICP-mass spectrometry (ICP-MS), after $HNO_3$ + HF digestion of 0.1000 g of sample powders in a Teflon-lined vessel at ~180 °C and 200 psi for 30 min, evaporation to dryness, and subsequent dissolution in 100 ml of 4 vol.% $HNO_3$. Trace element measurements were carried out in triplicate with a PE SCIEX ELAN-5000 spectrometer using rhodium as an internal standard. Precision, as determined from standards WSE, BR and AGV, analyzed as unknowns, was better

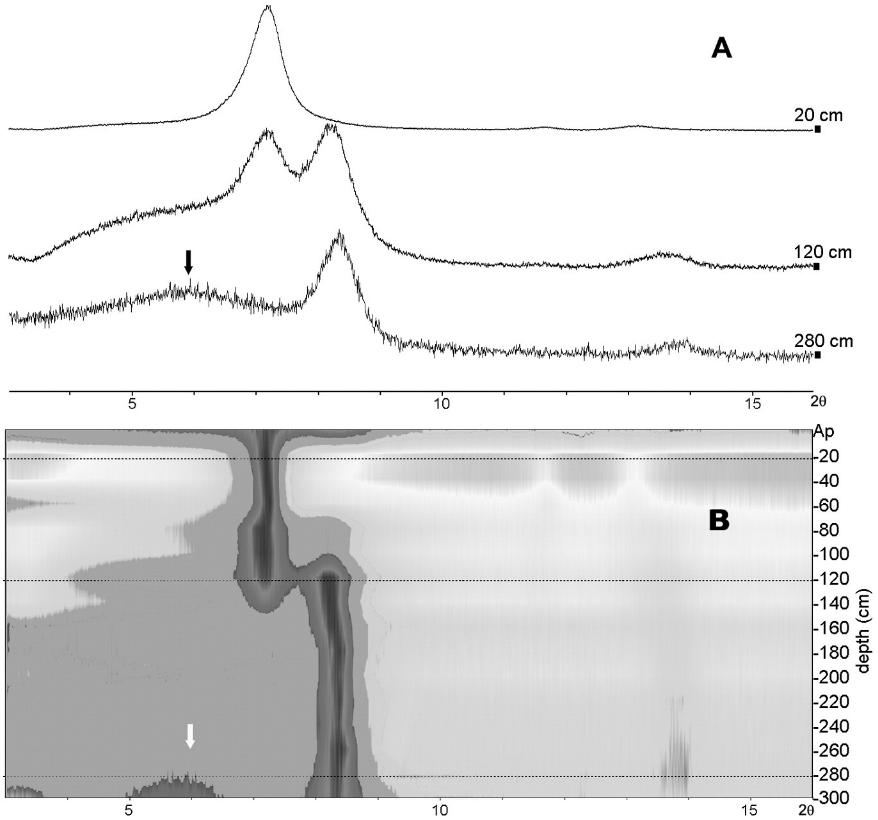

**Fig. 5.** XRD diagrams of oriented mounts of samples at 20, 120 and 280 cm (A), and grayscale map drawn from the overall XRD patterns sequence (B). The three XRD diagrams in A are marked by dotted lines in B. Grey levels of the map correspond to the relative intensity of XRD peaks. The change in the intensity of the main peaks (sepiolite at 7.2 °2θ, palygorskite at 8.2 °2θ, and smectite, indicated by arrows, at ~6 °2θ) indicate the distribution of clay minerals with depth (y-axis).

than ±2% and ±5% for analyte concentrations of 50 and 5 ppm, respectively.

Powder XRD analysis of the same specimens (decarbonated samples and Bt sample that did not contain carbonates) was carried out in the conditions specified above. The relative distribution of clay minerals and quartz was assessed from these powder X-ray patterns by measuring the integrated area of intense peaks of the mineral phases (110 for sepiolite, 110 for palygorskite, 001 for smectite, 100 for quartz) with the GRAMS/AI program. The presence of non-crystalline material was deduced in some of the XRD patterns from the background elevation between 20 and 40 °2θ. The area of such background elevation was used to assess non-crystalline phase contents. Oriented mounts were also prepared from the same samples. Parts of the powders were dispersed in distilled water and a few drops of the dispersion were placed onto a glass slide. The oriented mounts were analyzed with the same apparatus and conditions indicated above, excepting a narrower scan range of 3–30 °2θ. The XPOWDER program (Martín-Ramos et al., 2012) was used for XRD pattern visualization and to generate a gray-scale image of the XRD pattern sequence along the studied profile.

The decarbonated samples from three depths at 60, 160 and 200 cm were selected for transmission electron microscopy (TEM) because of their sepiolite, palygorskite and smectite contents previously determined by XRD. Samples were suspended in ultrapure ethanol and deposited on a copper grid coated with carbon. Quantitative analytical electron microscopy (AEM) was obtained with a Philips CM20 instrument operated at 200 kV and equipped with an EDX model EDAX. Analysis of sepiolite, palygorskite and smectite, was performed in scanning transmission electron microscopy (STEM) mode using a beam 5 nm in diameter and a scanning area of 20 × 100 nm. For quantitative microanalyses, EDX data were corrected using the thin-film method of Lorimer and Cliff (1976). The k-factors were determined using muscovite, albite, biotite, spessartine, olivine, and titanite standards.

## 4. Results

### 4.1. XRD study

The XRD investigation of the whole-rock soil profile shows that it is dominated by calcite and dolomite (Fig. 2), that there is a marked increase of carbonates in depth, and that there is a reversed distribution of calcite and dolomite along the profile (Fig. 3A). The dolomite in the studied profile is nearly stoichiometric, containing from 58 mol% $CaCO_3$ in the upper levels to 53 mol% $CaCO_3$ in the lower ones, as determined from the d-spacing of the 104 XRD peak according to Lumsden (1979).

In the decarbonated samples it was possible to investigate the silicate minerals present. From bottom to top, the XRD pattern sequence of powder samples of these decarbonated specimens (Fig. 4) indicates the following: Palygorskite is most abundant at the lower part of the profile, progressively decreasing upwards and disappearing at 60 cm. Smectite and non-crystalline material occur mainly at the bottom of the profile. Sepiolite appears constrained to the Bkkm1 horizon coexisting with palygorskite between 140 and 80 cm. Quartz decreases upwards and disappears at 60 cm. The Ap represents a reworked horizon, evidenced by the mixture of palygorskite, sepiolite and quartz. The reddish lenses (Bt), which did not contain any carbonates, occurring close to the bottom of the profile have a mineralogical composition similar to the decarbonated sample at 280 cm.

According to the above data there is an inverted distribution between the mineral pairs calcite–sepiolite and dolomite–palygroskite (Fig. 3A, B). Sepiolite proportion is highest between 40 and 60 cm. Smectite and non-crystalline material are observed in the deepest levels (Fig. 3C). Quartz is particularly abundant in the Ap horizon, disappears between 20 and 60 cm and shows a smooth increase with depth below 60 cm. The silicate mineralogy in the Bt lenses (clays, quartz,

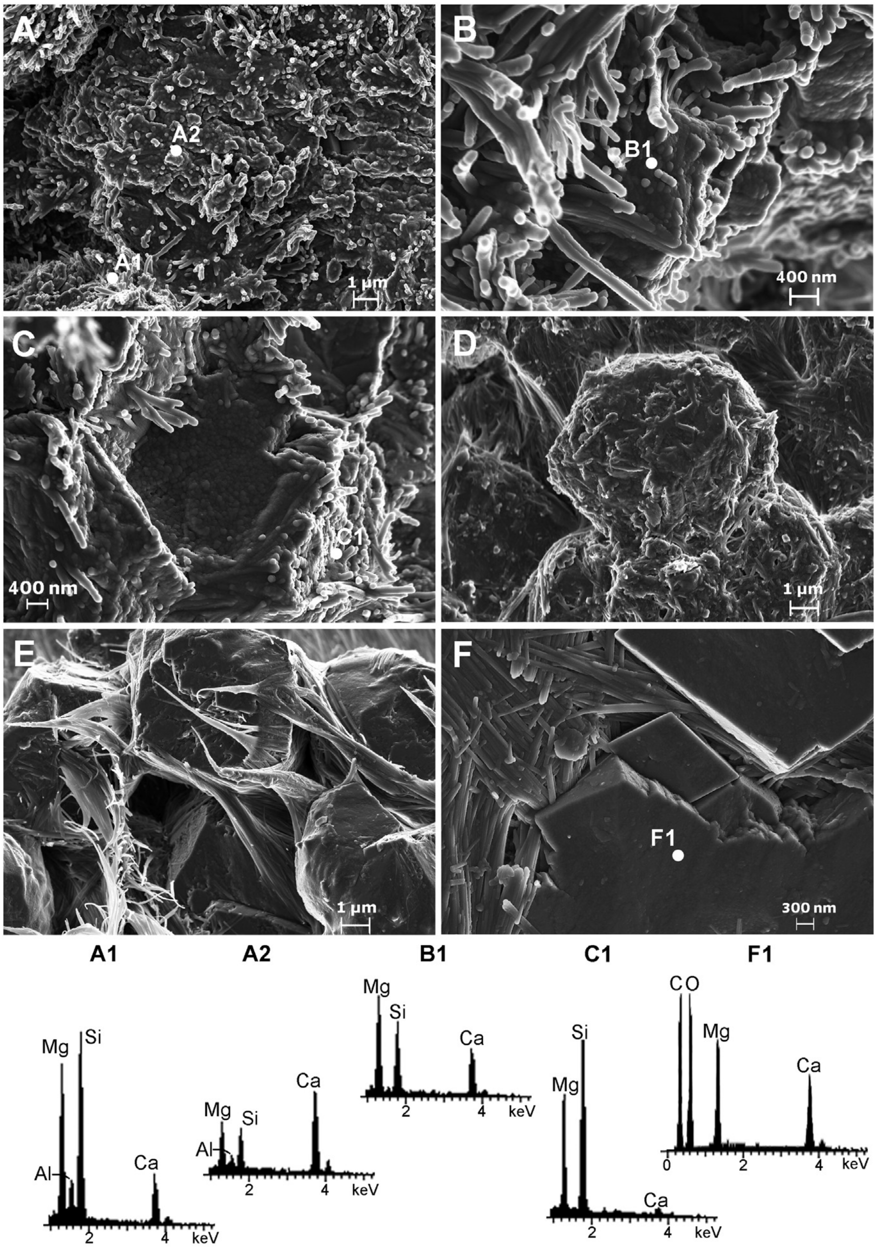

**Fig. 6.** SEM images (secondary electrons) and EDX spectra from soil samples at 60 (A), 100 (B and C) and 300 cm depth (D, E and F). A) Sepiolite filaments covering a substrate composed by nanometre-sized carbonate grains (calcite and dolomite). B) Fibrous sepiolite including an embryonic dolomite rhombohedron (center of the figure) with rounded crystal-growth units on its surface. C) Sepiolite-palygorskite filaments tightly intergrown with subhedral dolomite crystals. D) Dolomite rhombohedra completely covered by palygorskite fibres. E) Bundles of palygorskite fibrils coating dolomite crystals. F) Palygorskite fibres between dolomite crystals with flat surfaces. EDX spectra at the bottom correspond to dots in the images and indicate sepiolite-palygorskite fibres (points A1 and C1), areas containing carbonates and clays (A2: calcite; B1: dolomite) and only dolomite (F1).

and non-crystalline material) is very similar to that of the decarbonated samples at 280 cm (Fig. 3B, C).

The analysis of oriented mount preparations shows very clearly the confinement of sepiolite and palygorskite to the upper and lower part of the profile, respectively, the occurrence of a narrow zone of coexistence of these two phases, and the location of smectite close to the basaltic substrate and, in low concentration, at the surficial Ap horizon (Fig. 5).

### *4.2. SEM study*

The electron microscopy study of whole-rock specimens reveals that the clay minerals consist of sepiolite and palygorskite tightly intergrown with dolomite and calcite (Figs. 6, 7 and 8). The interpretation of the identity of the minerals observed and analyzed with SEM–EDX is helped by the XRD data above. At the upper levels of the profile, calcite and dolomite form small aggregates with a rough surface covered by sepiolite fibres (Fig. 6A, 6 spectrum A1, and Fig. 7A). The presence of calcite is indicated by the intense Ca peaks in the EDX spectra (Fig. 6A, spectrum A2), and dolomite by the intensity of Mg peaks in the same spectra, that cannot be accounted for by the clays alone (Fig. 6A, spectra A1 and A2). Sepiolite and palygorskite are characterized by the spectra with high Si and Mg, and low Al (Fig. 6, EDX spectra). In the intermediate levels of the profile, the dolomite crystals continue growing by the aggregation of rounded crystal units, and they are wrapped in fibers of both palygorskite and sepiolite (Figs. 6B, C, and 7B). EDX spectra of the dolomite rich areas show intense Mg and Ca peaks (Fig. 6B, spectrum B1). Lower in the profile, dolomite rhombohedra are covered by very small fibres of palygorskite (Figs. 6D and 7C) or appear enveloped by thin films constituted by bundles of palygorskite

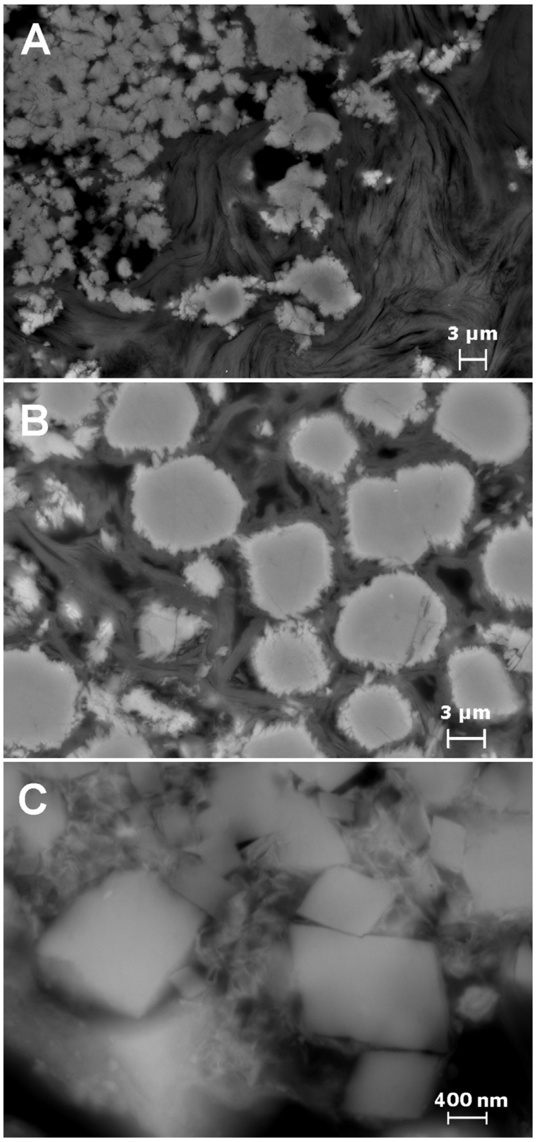

**Fig. 7.** SEM back-scattered electron (BSE) images showing dolomite crystal growth features and dolomite relation to clay minerals from soil samples at 60 (A), 100 (B) and 300 cm depth (C). A) Sepiolite including dolomite aggregates of very small particles. B) Dolomite crystals with rough surfaces surrounded by fibrous clays. C) Palygorskite fibres between dolomite rhombohedra. Notice the smaller scale bar in this picture.

microfibrils (Fig. 6E). In the deepest levels, palygorskite forms dense fibre alignments located in the voids between well-shaped dolomite crystals (Fig. 6F, spectrum F1). In summary, palygorskite found in the deepest levels occurs with mature dolomite, whereas at the top of the profile sepiolite coexists with calcite and dolomite of much smaller particle size.

An investigation of the mineral texture with less magnification shows that, in the upper profile levels, small dolomite crystals form circular or toroid-like aggregates wrapped in sepiolite (Fig. 8A, B). Dolomite coexisting with massive calcite at 100 cm is generally constituted by more mature crystals developed in close contact with palygorskite (Fig. 8C). At the deepest levels, very small relict tephra particles, partially transformed to clays (probably smectite, see below), are preserved within the dolomite crust (Fig. 8D).

### 4.3. Chemical petrography

The relation between textures and mineral compositions was investigated using EPMA for soil samples at 60 and 100 cm depth. The element maps consist of the intensity of the X-ray signal of K lines of the elements (as number of counts). The EPMA study of the dolomite-sepiolite spherules occurring at 60 cm (Fig. 8A and B) shows a marked Si and Mg enrichment at the rims, while Ca and Mg are abundant at the cores (Fig. 9A–C). This chemical distribution marks the presence of sepiolite and dolomite at the rims and core, respectively (Fig. 9D and E).

At 100 cm, the texture is very different. This specific depth was chosen because it contains all the minerals of interest (Fig. 3). X-ray element maps allow the visualization of “ghosts” of the original tephra grains altered to a different extent (Fig. 10). The elements that define the outline of these “ghosts” are K, Ti and Fe (Fig. 10), all of which have a similar spatial distribution. At the centre of these altered tephra grains, there is smectite (Fig. 11), where the concentration of these three elements is highest. Palygorskite also occurs within the relict tephra grains, close to the rims (Fig. 11). Sepiolite occurs in the interstitial space between the relict tephra grains (Fig. 11).

Three distinct Ca–Mg carbonates can be distinguished from the composition ternary diagram: Calcite, Mg-calcite and dolomite (Fig. 12A). Dolomite occurs within the relict tephra grains as rounded micrograins. Calcite occurs in the interstitial space between the silicate particles as sparitic grains (Fig. 12B). The Ca–Mg–Si triangle in Fig. 12A contains analyses with intermediate composition between clay, calcite and dolomite (pixels extending towards the Si apex). In the mineral phase map (Fig. 12B), only the pixels within the calcite, Mg-calcite and dolomite fields are represented.

The gray areas in Figs. 11 and 12 correspond to material that does not have the composition of either of the phases mentioned above (smectite, palygorskite, sepiolite, dolomite and calcite), mainly to unaltered or partially altered volcanic tephra (see also Fig. 10). EPMA quantitative single-spot analyses of clay minerals (Table 1) have been plotted in the $SiO_2$–$Al_2O_3$–MgO triangular diagram (squares in Fig. 11A). The number of pixel analyses in Fig. 11A has been reduced to mark only the clays composition, and corresponds to ~1/3 of the pixels in the map. Compositions between the smectite, palygorskite and sepiolite fields defined by these single-spot analyses correspond to mixtures of individual clays or perhaps partially altered tephra (band defined by pixels in Fig. 11A), although we do not think the latter amount to a significant proportion. The structural formulas of the clays (Table 1) indicate that Ti, Fe and K concentrate in smectite. The smectite composition is that of an Fe-rich montmorillonite, with similar proportions of Al, Mg and Fe, and a dioctahedral character. The tetrahedral substitution is high but the layer charge remains within the smectite limits. The playgorskite formulas indicate low tetrahedral substitution, Mg as the main octahedral cation, followed by Al and Fe, and thus a dominantly trioctahedral character. The interlayer charge is typically low. The sepiolite formulas indicate very high tetrahedral Si and octahedral Mg, with a variable interlayer charge.

### 4.4. AEM data

AEM analyses of the clays show some differences with those from EPMA, which is not surprising given the much smaller size of the analyzed area and the typical heterogeneity of clay composition. Also, the analyses are from different depths in the soil. The AEM analyses of the clays correspond to sepiolite at 60 cm, palygorskite at 160 cm and smectite at 160 and 200 cm, because the individual clays were concentrated at the corresponding depths. Sepiolite from the sample at 60 cm (Table 2) appears close to the Mg, trioctahedral end member (8 octahedral cations per formula unit, a.p.f.u.) but octahedral substitution of Al or Fe for Mg reduces Mg to less than 6 a.p.f.u in two cases. There is no tetrahedral substitution. A slight Si excess is observed in some analyses, which indicates the occurrence of an invisible Si-rich phase intergrown with the sepiolite fibers at TEM scale, most probably amorphous silica, which occurs frequently in combination with sepiolite and palygorskite (Birsoy, 2002; Robins et al., 2012). Those analyses with very small Si

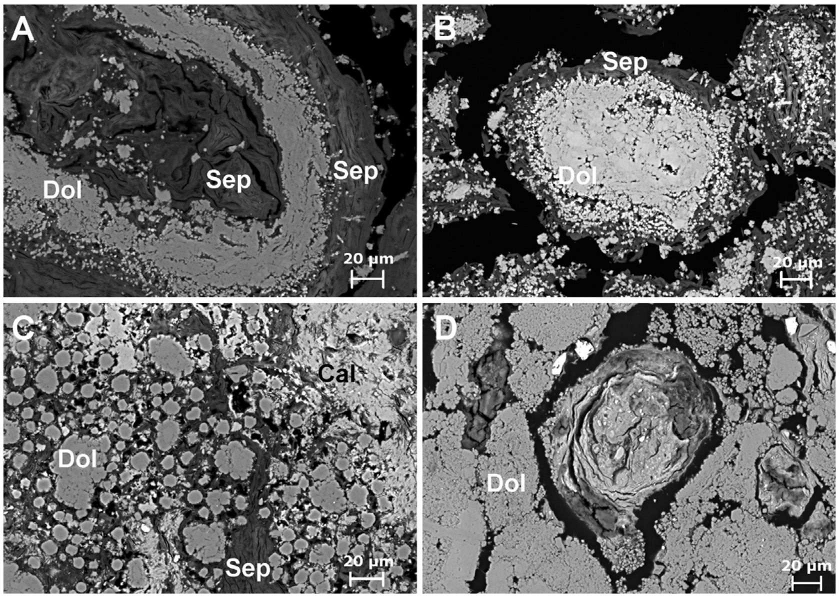

**Fig. 8.** SEM BSE low-magnification images showing the texture and distribution of carbonates in soil samples at 60 (A and B), 100 (C) and 300 cm depth (D). A) Spherule with a sepiolite (Sep) core and rim, and a dolomite (Dol) intermediate ring. B) Spherule with dolomite in the centre and a sepiolite rim. Variation of grey levels within the carbonate is related to Mg/Ca ratios, with lighter grey corresponding to lower Mg/Ca ratios. C) Micron size dolomite nodules and irregular calcite (Cal) particles included in a sepiolite-rich matrix. D) Dolomite crust including a relic of a small tephra particle partially altered to clays in its rim.

excess were corrected for it and appear in Table 2 (correction is <0.1 a.p.f.u of Si). Other analyses with larger Si excess are omitted in Table 2. No exchangeable cations were detected in the sepiolite particles at 60 cm with AEM (Table 2), although they were with EPMA at 100 cm (Table 1). Some AEM analyses of palygorskite also showed a Si excess and the analyses were only used if the correction was <0.1 a.p.f.u. of Si (Table 2). In palygorskite, there is low tetrahedral substitution and a marked substitution of Al for Mg in the octahedral sheet. This substitution is higher in AEM data from 160 cm than in EPMA results from 100 cm. The interlayer charge is also very low in the AEM analyses of palygorskite.

In agreement with EPMA data, AEM analyses indicate that the smectite from the lower levels (160–200 cm) is essentially an Fe-montmorillonite. A significant nontronitic component is observed in

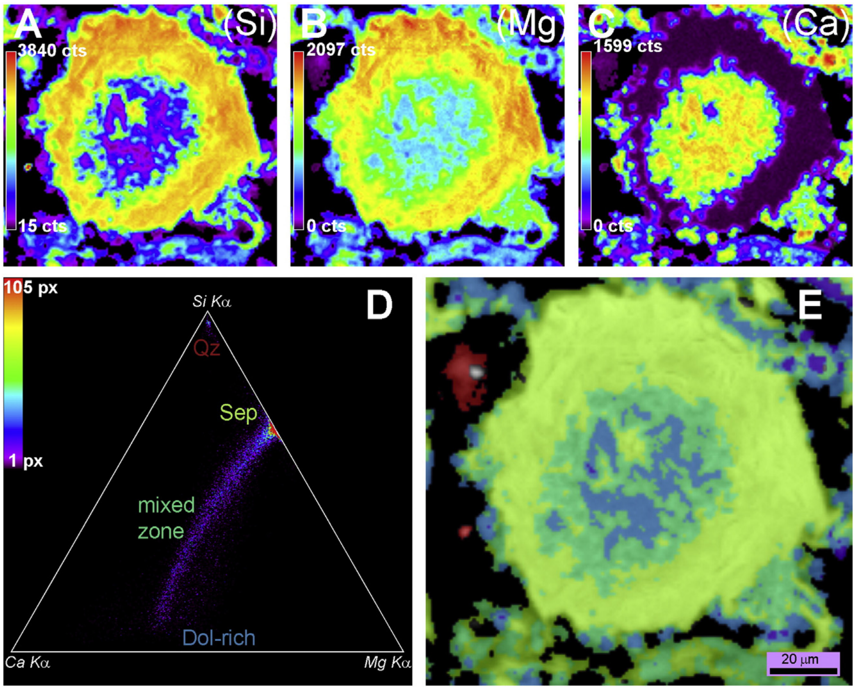

**Fig. 9.** Si (A), Mg (B) and Ca (C) X-ray (Kα) distribution maps of a spherule from a sample located at 60 cm depth. Color scales represent counts (cts) with warmer colors representing more intense X-ray signals. D) Triangular diagram of the Si–Ca–Mg chemical domain corresponding to the same image. The color indicates number of pixels with the specific chemical composition (see scale). E) Mineral phase map in the same image. The colors indicate the mineral phases represented in D: sepiolite (light green) surrounds the spherule, dolomite (blue) is located in the core, mixed with some sepiolite, probably below the analyzed surface (notice that in D data points close to dolomite composition have a Si component). An intermediate region with tightly intergrown sepiolite and dolomite is also represented (blue-green). Two quartz grains are in red.

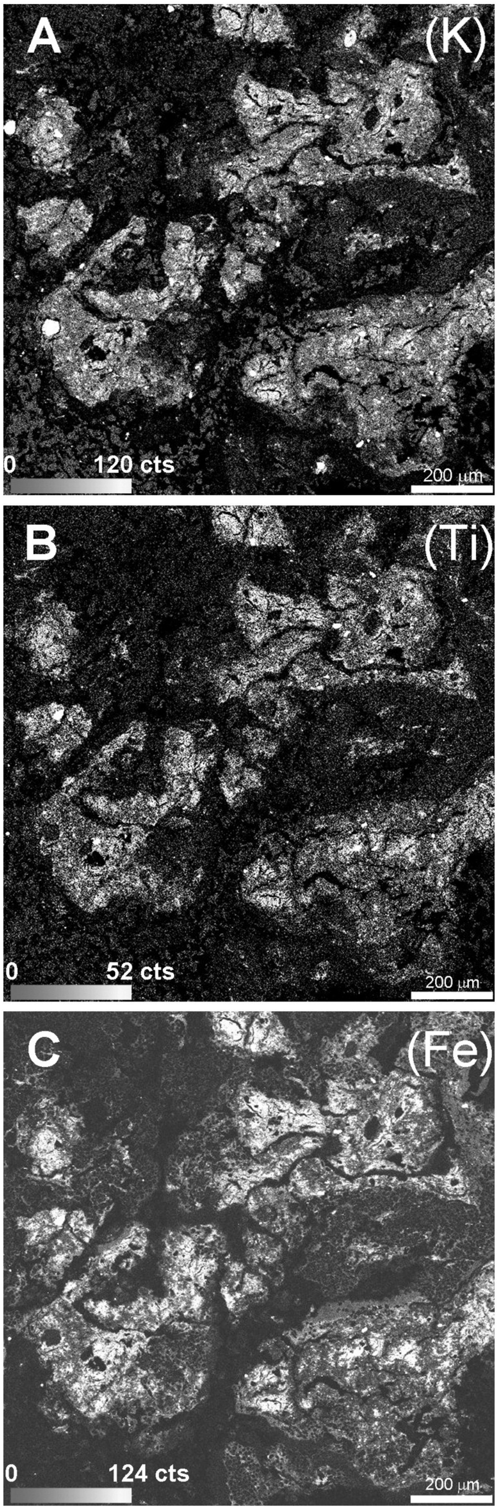

**Fig. 10.** Images of K (A), Ti (B) and Fe (C) X-ray (Kα) distribution maps of a sample at 100 cm depth. The grayscale represents the number of counts (cts). The lighter greys delineate "ghosts" of the original volcaniclastic textures, preserved after alteration.

one of the analyses, where Fe is 1.28 a.p.f.u. The main interlayer cation is K. No Na was detected in any of the clays using AEM.

### 4.5. Major and trace element geochemistry

Major and trace element contents (XRF data) from the decarbonated samples of the soil profile, from one sample corresponding to the substrate basalt at 320 cm and from a Bt sample (240–300 cm depth) are given in Table 3. The concentration profile of some of the major and trace elements are shown in Fig. 13. A marked $SiO_2$ and MgO enrichment occurs at the upper levels of the studied profile, with the exception of the reworked Ap horizon (Fig. 13A, B and Table 3), which correlates with the occurrence of sepiolite in these horizons. On the contrary, $K_2O$, $TiO_2$, $Fe_2O_3$ and $Al_2O_3$ are depleted in the range 20–140 cm and then increase progressively with depth to reach values similar to those of the underlying basalt (Fig. 13C, D), with the exception of $K_2O$, which is lower in the basalt than in the decarbonated samples below 80 cm. The $K_2O$ concentration at the lower part of the soil profile is probably controlled mainly by smectite (Fig. 3C), which has K as the main interlayer cation (Tables 1 and 2). The content of $TiO_2$ and $Fe_2O_3$ reaches the highest values in the substrate basalts. The reworked Ap horizon contains K, Ti, Fe and Al in higher proportion than the horizons immediately below and in similar proportion to those in the lower horizons.

Trace elements such as Li and Rb have a concentration distribution parallel to that of K (Fig. 13E, F), probably because they substitute for K in smectite. The concentration of REE is highest in the reworked Ap horizon, the basalt and the Bt samples (Fig. 13G). REE and HFSE (Nb, Ta, Zr, Hf) distributions are similar to those of Fe and K, respectively. The Bt lenses have a chemical composition similar to the decarbonated sample at 280 cm.

## 5. Discussion

### 5.1. Characteristics of the soil profile

The studied soil profile has the general characteristics expected from an arid or semiarid environment. Both massive carbonate precipitation and authigenic sepiolite and palygorskite are typical of such environments (Chamley, 1989; Robins et al., 2012). However, given that the volcanic activity that generated the tephra on which the soil originated goes back to 3 My–3 ky (Guillou et al., 2004; Rodríguez-González et al., 2012) there is a large span of time in which climatic conditions changed. The last hundreds of thousands of years have been of prevalent arid or semiarid conditions alternating with more humid periods (Moreno et al., 2002). In consequence the soil may be the result of a complex cycle of environmental conditions and processes. During the arid-semi arid periods, calcite and dolomite precipitated massively after the dissolution of Ca, Mg-rich silicate minerals of the volcanic parent material accelerated by reaction with the $CO_2$ released in the soil by microbial and plant respiration and by organic matter decay.

The upper part of the soil (approx. 0–170 cm deep), consisting of the surface Ap horizon and the Bkkm1 horizon (Fig. 1), a calcitic caliche, can be considered as a Typic Petrocalcid (Soil Survey Staff, 2014). The lower part of the profile is a thick dolomite caliche (Bkkm2 and Bkkm3 horizons, Fig. 1) including Bt lenses. Mineralogical and geochemical data of the studied profile provide the main following information: 1) sepiolite and palygorskite are the main clay minerals in the profile, with sepiolite dominating the upper part of the Bkkm1 horizon and palygorskite the lower part of the profile (Figs. 3B and 4); 2) smectite occurs in the lowest part of the Bkkm3 horizon (Figs. 3C and 4); 3) calcite and dolomite occur in the profile with a distribution in which calcite is more abundant in the upper part of the profile and dolomite entirely dominant in the lower part (Figs. 2 and 3A); 4) dolomite occurs always in a close intergrowth with sepiolite or palygorskite (Figs. 7, 9 and 12), whereas calcite occurs in the pore space between clays or partially altered tephra (Fig. 12); 5) dolomite crystals grow with depth (Figs. 6, 7), apparently by merging of crystals (Fig. 8); 6) there is a Si and Mg enrichment at the top of the profile, excepting the Ap horizon (Fig. 13), which is, roughly, inversely correlated with the concentration of Ti, Fe, Al, K, HFSE, LILE and REE in the profile (Fig. 13, Table 3); and 7) the mineralogy and geochemistry of the Bt lenses is similar to those of the decarbonated soil at the same depth (Fig. 3B–C, 4, and 13).

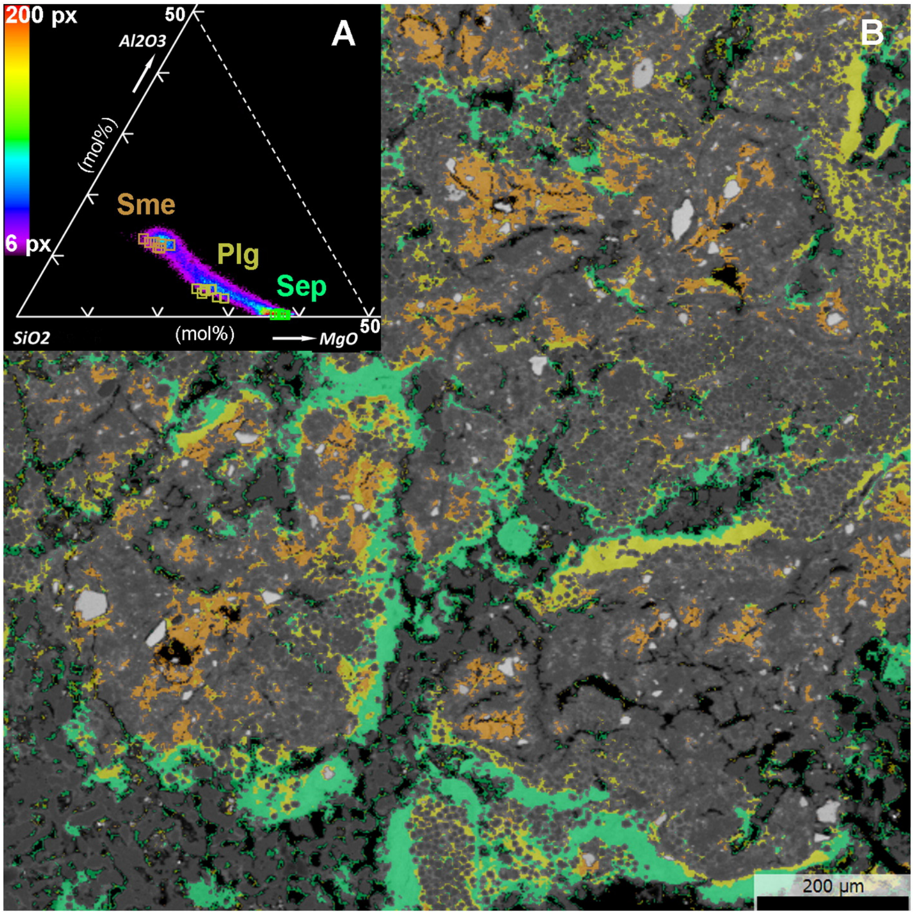

**Fig. 11.** Clay mineral composition from EPMA. A) Composition of clay minerals in the image in B, from the sample at 100 cm depth, plotted in the ternary diagram $SiO_2$–$Al_2O_3$–MgO (molar proportions). Squares correspond to single-spot EPMA analyses of smectite (orange), palygorskite (yellow) and sepiolite (green). Pixels correspond to the composition of the same clay minerals obtained from element X-ray maps. Pixels with compositions away from the clay field have been removed for clarity. The pixel colors indicate the number of pixels with a specific composition (see color scale). B) Mineral phase map of the same area shown in Fig. 10. Smectite (orange) is located in the innermost zones of the altered tephra grains, palygorskite (yellow) near the grain rims and sepiolite (green) in the interstitial space between grains.

### *5.2. Soil silicate mineralogy and formation processes*

The chemical composition of the original volcanic material where the soil developed can be deduced from the major and trace elements distribution in the profile (Fig. 13). The two most immobile major elements are Al and Fe, and they provide the main clue for constraining the composition of the volcanic material. These two elements have a maximum and approximate constant concentration at the interval 160–300 cm in the profile and at the Ap horizon at the top of the profile (Fig. 13). The point at 320 cm corresponds to unaltered basalt, which is not part of the soil. Iron and Al concentrations decrease considerably in the interval 20–140 cm. This decrease is very unlikely due to Al or Fe depletion, given their immobile character. Rather, their decrease is due to addition of Si and Mg to the profile, given that the Si and Mg increase in this area exactly mirrors Al and Fe decrease. Silicon and Mg are mobile cations and we interpret that they travelled with the runoff from upper parts of the long slope on which the studied location is placed (Fig. 1C). The basalt and tephra in this slope (Fig. 1B) is an evident source of Si, Mg and Ca that can travel dissolved in surficial, percolating waters. Silicate and carbonate phases precipitated in the soil down the slope from these solutions. It would have been possible that the large sepiolite content at the top of the profile (Fig. 3B) was generated by deposition of sepiolite formed somewhere else. However, clay could have been illuviated only at the early stages of the soil development (carbonate cementing stages I to early III of Gile et al., 1966), before the development of the physical barrier represented by the petrocalcic horizon (stage IV of Gile et al., 1966). Clay crystallizes slowly, especially in arid climates (even now, the transformation of the tephra into clay is not complete), which means that there was less clay to be transported in the early stages of soil formation when illuviation was physically possible. The large sepiolite presence in the upper parts of the profile does not support illuviation at an early stage only. Moreover, from the textural perspective, illuviation of sepiolite is unlikely because the circular and concentric structures (Fig. 8A, B) and the microfabric within the range 20–100 cm (Figs. 6, A-C, and 7A, B) suggest also co-precipitation of sepiolite with dolomite.

The concentrations of major elements in the Bt lenses without carbonates are similar or coincident to those of the decarbonated soil at the same depth (Fig. 13A–D). Thus, the composition of the original tephra can be considered to be that of the decarbonated soil at 0, at 160–300 cm and that of the Bt lenses, for which Fe and Al remain approximately constant, indicating a conservative weathering process of the tephra. This composition is less mafic than that of the underlying basalt because Si and K are higher in the tephra, and Mg, Fe and Ti are higher in the basalt (Fig. 13). The above interpretation is compatible with the concentration distribution of some of the trace elements such as Li, Rb and HFSE, which are higher in the tephra than in the basalt, and of the REE, which is higher in the underlying basalts (Fig. 13, E-H). HFSE and Rb also display approximately constant concentrations in the Ap horizon and between 160 and 300 cm, mirroring the behaviour of Al and Fe.

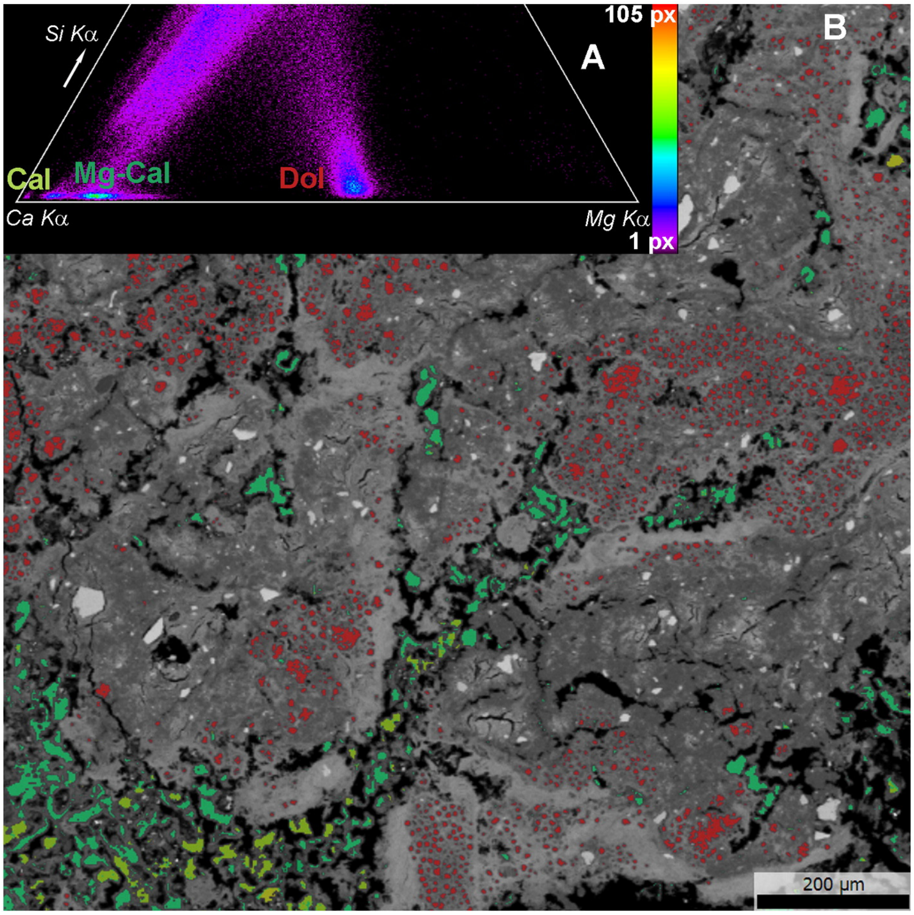

**Fig. 12.** Carbonate mineral composition from EPMA data corresponding to the same area in Figs. 10 and 11. A) Zone of the Si–Ca–Mg triangular diagram containing the carbonate mineral compositions: calcite (Cal), Mg-calcite (Mg–Cal) and dolomite (Dol). The pixel colors indicate pixel density in the chemical field. All chemical compositions obtained are shown. B) Mineral phase map showing dolomite (red) within the altered tephra, and calcite (light green) and Mg-calcite (dark green) in the interstitial space between grains.

Palygorskite is the main silicate mineral phase in the lower part of the profile (Figs. 3B and 4), where the conservative weathering process took place. Thus, palygorskite is the result of in situ alteration of the tephra without major cation addition or depletion. On the contrary, sepiolite is dominant in the upper part of the profile, indicating that sepiolite formation is connected with the massive Si and Mg input at the top (see sepiolite composition in Tables 1 and 2). Obviously, calcite and dolomite imply also a massive input of Ca and Mg across the entire profile (Fig. 3A). Quartz relative abundance in the profile supports this interpretation. Quartz is hardly detectable in the samples where sepiolite predominates and becomes more abundant at depths where palygorskite is relatively more abundant (Fig. 4). The explanation is that quartz was present in the original tephra or is a product of the in situ alteration of the tephra. At those levels (20–120 cm) where there was a large addition of exogenic Si and Mg the precipitation of sepiolite dilutes quartz in the soil and it becomes undetectable. In the XRD patterns of the decarbonated soil, the traces where quartz is not observable (20–60 cm, Fig. 4) are those that have the highest signal-to-noise ratio, indicating that the amount of crystalline material in these samples is the highest. This is so because of the large sepiolite addition (precipitated from exogenic Mg and Si) to these soil horizons, that generates very intense sepiolite peaks and dilutes all the minerals existent or generated in situ.

The link of palygorskite and sepiolite to a conservative and non-conservative alteration of the tephra, respectively, is supported by the textural information also. In the upper part of the profile there are numerous rounded sepiolite structures wrapping dolomite (Figs. 8A, B and 9). These structures decrease in abundance downwards in the profile in a transition where the original tephra is more frequently recognized, texturally and chemically (Figs. 10 and 11). This is consistent with precipitation of sepiolite in the upper part from exogenous Mg and Si, and with palygorskite formation from conservative alteration of the tephra.

The detailed investigation of the chemistry and texture of a sample from 100 cm depth, carried out by EPMA, confirms this interpretation. This sample is important because it contains sepiolite, palygorskite, calcite, and dolomite, all in sufficient amount (Fig. 3A, B), for a representative investigation of the mineral distribution within the soil fabric. The characteristic observation from the 100 cm sample is the existence of partially altered tephra grains and pores between them (Fig. 11). Smectite appears within the tephra grains (orange areas in Fig. 11), as a result of their alteration. Although there are significant areas corresponding to smectite in the analyzed images (Fig. 11), the overall smectite abundance in the sample from 100 cm is lower than those of palygorskite and sepiolite, as indicated by XRD (Fig. 4). Sepiolite (green areas in Fig. 11) appears clearly situated in the pore space between relict tephra grains. The location of palygorskite (yellow areas in Fig. 11) appears as intermediate between those of smectite and sepiolite, near or at the edges of the grains, associated with sepiolite, and within the grains, associated with smectite (Fig. 11). This mineral distribution is perfectly coherent with the interpretation of the processes based on the geochemistry of the profile (Fig. 13). At 100 cm, there is a clear chemical indication of exogenous Si and Mg (Fig. 13). The interstitial sepiolite is the result of precipitation from fluids carrying Si and Mg both from

**Table 1**
Structural formulas of clay minerals from soil samples at 100 cm depth, from EPMA single-spot analyses.

| | Sepiolite | | | | | | Palygorskite | | | | | | | Smectite | | | | | | | | |
|---|---|---|---|---|---|---|---|---|---|---|---|---|---|---|---|---|---|---|---|---|---|---|
| Si | 12.00 | 12.00 | 11.98 | 11.96 | 11.90 | 11.88 | 8.00 | 7.90 | 7.76 | 7.87 | 7.94 | 7.96 | 7.96 | 3.53 | 3.64 | 3.60 | 3.56 | 3.59 | 3.48 | 3.58 | 3.72 | 3.71 |
| $Al^{IV}$ | 0.00 | 0.00 | 0.02 | 0.04 | 0.09 | 0.12 | 0.00 | 0.10 | 0.24 | 0.13 | 0.06 | 0.04 | 0.04 | 0.47 | 0.36 | 0.40 | 0.44 | 0.41 | 0.52 | 0.42 | 0.28 | 0.29 |
| $Al^{VI}$ | 0.06 | 0.07 | 0.11 | 0.07 | 0.00 | 0.02 | 0.96 | 0.92 | 0.80 | 0.58 | 0.69 | 1.04 | 0.96 | 0.66 | 0.74 | 0.67 | 0.64 | 0.75 | 0.61 | 0.78 | 0.79 | 0.80 |
| Fe[a] | 0.04 | 0.04 | 0.08 | 0.13 | 0.06 | 0.08 | 0.38 | 0.38 | 0.38 | 0.32 | 0.33 | 0.04 | 0.05 | 0.65 | 0.57 | 0.63 | 0.65 | 0.57 | 0.63 | 0.62 | 0.56 | 0.54 |
| Mg | 7.61 | 7.37 | 7.63 | 7.63 | 7.91 | 7.78 | 2.90 | 3.01 | 2.91 | 3.62 | 3.41 | 2.85 | 3.05 | 0.70 | 0.70 | 0.72 | 0.71 | 0.65 | 0.76 | 0.55 | 0.60 | 0.58 |
| Ti | 0.00 | 0.00 | 0.02 | 0.04 | 0.01 | 0.01 | 0.01 | 0.02 | 0.03 | 0.02 | 0.01 | 0.01 | 0.01 | 0.17 | 0.15 | 0.16 | 0.15 | 0.15 | 0.17 | 0.16 | 0.14 | 0.15 |
| $\Sigma^{VI}$ | 7.72 | 7.49 | 7.82 | 7.84 | 7.97 | 7.89 | 4.25 | 4.32 | 4.11 | 4.53 | 4.45 | 4.24 | 4.31 | 2.18 | 2.16 | 2.18 | 2.15 | 2.13 | 2.17 | 2.11 | 2.09 | 2.07 |
| Na | 0.05 | 0.04 | 0.07 | 0.06 | 0.04 | 0.03 | 0.05 | 0.02 | 0.03 | 0.04 | 0.02 | 0.06 | 0.07 | 0.03 | 0.04 | 0.03 | 0.03 | 0.12 | 0.05 | 0.03 | 0.06 | 0.07 |
| K | 0.01 | 0.01 | 0.02 | 0.01 | 0.01 | 0.01 | 0.01 | 0.02 | 0.03 | 0.03 | 0.01 | 0.01 | 0.01 | 0.25 | 0.27 | 0.25 | 0.27 | 0.28 | 0.28 | 0.29 | 0.25 | 0.29 |
| Ca | 0.20 | 0.43 | 0.05 | 0.05 | 0.03 | 0.09 | 0.03 | 0.05 | 0.36 | 0.03 | 0.05 | 0.04 | 0.05 | 0.09 | 0.07 | 0.07 | 0.12 | 0.07 | 0.14 | 0.08 | 0.08 | 0.08 |
| Layer ch. | 0.45 | 0.91 | 0.19 | 0.17 | 0.12 | 0.22 | 0.13 | 0.13 | 0.78 | 0.13 | 0.13 | 0.14 | 0.17 | 0.44 | 0.45 | 0.41 | 0.54 | 0.54 | 0.60 | 0.48 | 0.46 | 0.52 |
| O | 34 | 34 | 34 | 34 | 34 | 34 | 22 | 22 | 22 | 22 | 22 | 22 | 22 | 12 | 12 | 12 | 12 | 12 | 12 | 12 | 12 | 12 |
| H | 4 | 4 | 4 | 4 | 4 | 4 | 2 | 2 | 2 | 2 | 2 | 2 | 2 | 2 | 2 | 2 | 2 | 2 | 2 | 2 | 2 | 2 |
| $H_2O$ | 4 | 4 | 4 | 4 | 4 | 4 | 4 | 4 | 4 | 4 | 4 | 4 | 4 | | | | | | | | | |
| Ch. balance[b] | 0.00 | 0.00 | 0.00 | 0.00 | −0.04 | 0.00 | 0.00 | 0.00 | 0.00 | 0.00 | 0.00 | 0.00 | 0.00 | 0.00 | 0.00 | 0.00 | 0.00 | 0.00 | 0.00 | 0.00 | 0.00 | 0.00 |

[a] Total Fe as $Fe^{3+}$.

[b] Difference between the charge of the interlayer cations and the layer charge calculated from the lattice cations.

percolating waters (exogenous ions) and from the tephra grains in situ, in the process of alteration. Smectite has the largest Al + Fe proportion of the three clay minerals (Tables 1 and 2). These two cations are immobile and thus smectite forms within the tephra grains, where Al and Fe are abundant. Palygorskite also contains Fe and Al, in a smaller proportion, and it forms preferentially within the grains.

### *5.3. Role of clays and volcanic tephra in the formation of dolomite*

The formation processes of the clay mineral phases needs now to be connected with that of the carbonates, which make up a large proportion of the soil, from ~15 to ~90% in weight (Figs. 2, 3A). The EPMA investigation shows that dolomite precipitates always within a clay or tephra matrix. In the upper part of the profile, dolomite is found within the round sepiolite structures (Fig. 9) and, deeper in the profile, within tephra grains or within sepiolite or palygorskite matrixes (red areas in Fig. 12; compare with Fig. 11 to see the silicate mineralogy). In contrast, calcite precipitates only in the space between tephra grains (green areas in Fig. 12). The same conclusion is obtained from SEM analysis. Observations include: dolomite wrapped in rounded sepiolite structures (Fig. 8B); small dolomite crystals within a clay matrix (Figs. 6 and 8C) and massive calcite in the space between other grains or structures (Fig. 8C); dolomite surrounded by clay fibers (Fig. 6D–F). As the dolomite crystals grow in size and dolomite proportion increases (up to ~90 wt.%; Fig. 3A), dolomite acquires a massive appearance (Fig. 8D) although finer palygorskite films still surround the growing crystals (Fig. 6D, E). Accordingly, calcite precipitates in the space at the grain boundaries and dolomite only confined within a clay matrix or weathering tephra grains.

The reason for such behaviour is connected with the so-called “dolomite problem” (Van Tuyl, 1916). Although dolomite is the most supersaturated carbonate in present seawater, there is very little evidence of dolomite precipitation in modern marine sediments. Specifically, modern dolomites are restricted to hypersaline lakes, lagoons and zones of microbial mediation where porewater alkalinity is very high (Vasconcelos and McKenzie, 1997; Arvidson and Mackenzie, 1999 and references therein). Dolomites from ancient sediments are abundant but they had a diagenetic origin (Deelman, 2011). There exists a kinetic control on the crystallization of dolomite vs. calcite. For a wide range of chemical conditions calcite precipitates much faster from solution and totally inhibits dolomite precipitation. Dolomite has not yet been precipitated from solution in ambient and inorganic conditions (Machel, 2004; McKenzie and Vasconcelos, 2009). The failure in the abiotic precipitation of dolomite in the laboratory and the discovery that bacteria promoted microenvironments that facilitate the precipitation of dolomite recently led researchers to suggest a link between dolomite formation and bacterial activity (e.g., Vasconcelos et al., 1995; Vasconcelos and McKenzie, 1997; Bontognali et al., 2008, 2010; Sánchez-Román et al., 2011), although the exact physico-chemical mechanisms for the bacterially-mediated precipitation of dolomite remain unknown. However, protodolomite precipitates from highly supersaturated solutions and then ages into dolomite (Kelleher and Redfern, 2002; Schmidt et al., 2005; Deelman, 2011; Diaz-Hernandez et al., 2013) with no bacterial mediation. Similarly, precipitation experiments of Ca–Mg carbonates mediated by bacteria indicated that the role of the bacteria for dolomite precipitation was simply that of producing $CO_2$ and generating a gel (biofilm) within which dolomite formation was catalyzed (Sanchez-Navas et al., 2009). The gel-like biofilm generates a high-viscosity medium where ion diffusion is slow and controlled by diffusive transport of ions. In such conditions, local supersaturation of solutes is facilitated (Henisch, 1989) and dolomite precipitation can take place. Rodríguez-Blanco et al. (2015) have discussed the mechanism of dolomite precipitation from supersaturated solutions through a three-step process involving formation of a hydrated nanoparticle precursor, transformation of the precursor into a protodolomite phase and the latter into dolomite. The morphology of the precursor and dolomite structures

**Table 2**
Structural formulas of clay minerals from AEM data, from samples at 60, 160 and 200 cm depth.

| | Sepiolite (60 cm) | | | | | | | | Palygorskite (160 cm) | | | | | | | Smectite (160 cm) | | | | Smectite (200 cm) | | | | | |
|---|---|---|---|---|---|---|---|---|---|---|---|---|---|---|---|---|---|---|---|---|---|---|---|---|---|
| Si | 12.00 | 12.00 | 12.00 | 12.00 | 12.00 | 12.00 | 12.00 | 12.00 | 7.95 | 8.00 | 7.90 | 8.00 | 8.00 | 8.00 | 8.00 | 3.42 | 3.67 | 3.76 | 3.52 | 3.63 | 3.86 | 3.43 | 3.58 | 3.70 | 3.51 |
| $Al^{IV}$ | | | | | | | | | 0.05 | 0.00 | 0.10 | 0.00 | 0.00 | 0.00 | 0.00 | 0.58 | 0.33 | 0.24 | 0.48 | 0.37 | 0.14 | 0.57 | 0.42 | 0.30 | 0.49 |
| $Al^{VI}$ | 0.73 | 0.40 | 0.27 | 0.81 | 0.28 | 0.40 | 0.29 | 1.00 | 1.76 | 1.15 | 1.34 | 1.59 | 1.47 | 1.40 | 1.68 | 1.12 | 1.04 | 0.88 | 0.64 | 1.51 | 1.30 | 0.89 | 1.89 | 1.42 | 0.58 |
| Fe[a] | 0.67 | 0.00 | 0.05 | 0.16 | 0.06 | 0.06 | 0.06 | 0.35 | 0.53 | 0.51 | 0.47 | 0.24 | 0.51 | 0.51 | 0.47 | 0.57 | 0.53 | 0.64 | 1.20 | 0.28 | 0.51 | 0.81 | 0.09 | 0.37 | 1.28 |
| Mg | 5.89 | 7.41 | 7.51 | 6.56 | 7.49 | 7.32 | 7.48 | 5.98 | 1.54 | 2.43 | 2.18 | 2.26 | 2.02 | 2.05 | 1.68 | 0.44 | 0.58 | 0.62 | 0.37 | 0.35 | 0.29 | 0.49 | 0.24 | 0.24 | 0.38 |
| $\sum^{VI}$ | 7.30 | 7.80 | 7.84 | 7.52 | 7.83 | 7.77 | 7.83 | 7.33 | 3.83 | 4.09 | 3.99 | 4.09 | 4.01 | 3.97 | 3.83 | 2.14 | 2.15 | 2.15 | 2.21 | 2.13 | 2.11 | 2.20 | 2.22 | 2.03 | 2.25 |
| K | | | | | | | | | 0.10 | 0.10 | 0.17 | 0.00 | 0.00 | 0.00 | 0.07 | 0.54 | 0.28 | 0.23 | 0.11 | 0.24 | 0.10 | 0.44 | 0.00 | 0.45 | 0.12 |
| Ca | | | | | | | | | 0.00 | 0.03 | 0.07 | 0.00 | 0.00 | 0.07 | 0.07 | 0.04 | 0.09 | 0.09 | 0.05 | 0.03 | 0.00 | 0.02 | 0.00 | 0.00 | 0.00 |
| Interlayer ch. | 0.00 | 0.00 | 0.00 | 0.00 | 0.00 | 0.00 | 0.00 | 0.00 | 0.10 | 0.17 | 0.30 | 0.00 | 0.00 | 0.14 | 0.20 | 0.61 | 0.46 | 0.41 | 0.21 | 0.31 | 0.10 | 0.48 | 0.00 | 0.45 | 0.12 |
| O | 34 | 34 | 34 | 34 | 34 | 34 | 34 | 34 | 22 | 22 | 22 | 22 | 22 | 22 | 22 | 12 | 12 | 12 | 12 | 12 | 12 | 12 | 12 | 12 | 12 |
| H | 4 | 4 | 4 | 4 | 4 | 4 | 4 | 4 | 2 | 2 | 2 | 2 | 2 | 2 | 2 | 2 | 2 | 2 | 2 | 2 | 2 | 2 | 2 | 2 | 2 |
| $H_2O$ | 4 | 4 | 4 | 4 | 4 | 4 | 4 | 4 | 4 | 4 | 4 | 4 | 4 | 4 | 4 | | | | | | | | | | |
| Ch balance[b] | 0.00 | 0.00 | 0.00 | 0.00 | 0.00 | 0.00 | 0.00 | 0.00 | 0.00 | 0.00 | 0.00 | 0.00 | 0.00 | 0.00 | 0.00 | 0.00 | 0.00 | 0.00 | 0.00 | 0.00 | 0.00 | 0.00 | 0.00 | 0.00 | 0.00 |

[a] Total Fe as $Fe^{3+}$.

[b] Difference between the charge of the interlayer cations and the layer charge calculated from the lattice cations.

found by Rodríguez-Blanco et al. (2015) (see their Fig. 6) is similar to that found in the present study, both in size and shape, and suggests similarities in the crystallization process even though the timing and conditions are very different.

In our soils, the fabric of the weathering tephra and of the sepiolite or paligorskite acts as a gel medium where ion supersaturation generates dolomite, perhaps following a multi-step process (Diaz-Hernandez et al., 2013). Certainly, the nm-size dolomite structures are seen to merge and become larger as the amount of dolomite increases down in the soil profile (Figs. 7A, B and 8). Calcite precipitates in the space between grains, even though there the amount of dissolved Mg was also high. Proof of the high Mg content of the pore solutions is the large addition of Mg to the soils at all heights. In the upper part of the profile this addition is obviously recorded in the silicate minerals as producing sepiolite precipitation (Figs. 3B and 13B). In the lower part of the profile, it is recorded in the large dolomite content (Fig. 3A) which required a Mg amount well above the original content of the tephra (Fig. 13B).

### 5.4. Clay-carbonate formation and thermodynamic constraints

The scheme of the caliche soil development presented here is consistent with thermodynamic considerations but our and previous results highlight the existence of other system constraints. Birsoy's (2002) investigation of the thermodynamics of the formation of palygorskite, sepiolite and associated carbonates shows that dolomite and palygorskite should precipitate together, while sepiolite and magnesite should precipitate together. This is entirely coherent because the Mg content increases from palygorskite to sepiolite and from dolomite to magnesite, which means that, all other conditions being equal, the pair sepiolite–magnesite requires higher Mg activity in solution to precipitate than the pair dolomite–palygorskite. However, Birsoy (2002) states that experiments and field evidence indicate that most times the precipitation of these phases is controlled by kinetic rather than thermodynamic factors. The formation of silicate and carbonate phases in our soils is obviously not controlled by thermodynamics for two reasons. One is that we find the pairs dolomite–palygorskite and sepiolite–calcite, whereas a purely thermodynamic control should produce dolomite–palygorskite and sepiolite–magnesite (Birsoy, 2002). The second reason is that, as discussed above, dolomite precipitation is controlled by kinetic constraints.

### 5.5. Soil formation and evolution

The mechanisms of clay and carbonate formation indicated by the chemical, textural and mineralogical data are probably not complete with the above description. The data in this study do not provide a temporal relationship between the formation of the clays and the carbonates except where dolomite is observed to grow within clay matrices. As arid conditions are favorable for carbonate precipitation and for sepiolite and palygorskite formation, it can be assumed that all these reactions were taking place together. However, clay formation is much slower than carbonate precipitation, and clays are also much more stable than carbonates in changing environmental conditions. Thus, it is possible that carbonate precipitation took place in several stages or even that there were cycles of carbonate precipitation and dissolution that did not affect the silicates.

The Bt lenses of the soil profile where no carbonates were present (Fig. 1D, E) are relevant in this sense. Were carbonates never precipitated there or were they precipitated and then dissolved in a subsequent stage? The chemistry of the Bt lenses is very similar to that of the decarbonated soil at the same depth (Fig. 13A–D), which does not suggest the activity of fluids focused on these areas. The silicate mineralogy at the investigated Bt lens has the lowest clay development of all the samples (Fig. 4), although very similar to that at 280 cm, the closest to the investigated Bt. The lower clay content suggests lower water access

**Table 3**
Major (%) and trace element (ppm) composition for surficial Ap horizon (0 cm depth), decarbonated samples (from 20 to 300 cm depth), underlaying basalt (320 cm depth) and Bt level (240–300 cm depth).

| | Ap | 20 | 40 | 60 | 80 | 100 | 120 | 140 | 160 | 180 | 200 | 220 | 240 | 260 | 280 | 300 | 320 | Bt |
|---|---|---|---|---|---|---|---|---|---|---|---|---|---|---|---|---|---|---|
| $SiO_2$ | 52.2 | 65.6 | 61.0 | 62.2 | 58.4 | 58.4 | 57.0 | 56.5 | 54.7 | 54.6 | 54.8 | 52.8 | 53.8 | 54.3 | 50.5 | 51.3 | 40.5 | 51.9 |
| $TiO_2$ | 2.4 | 0.3 | 0.2 | 0.1 | 1.1 | 0.9 | 1.7 | 1.9 | 2.2 | 2.4 | 2.4 | 2.5 | 2.5 | 2.2 | 3.2 | 2.8 | 3.5 | 3.2 |
| $Al_2O_3$ | 12.9 | 1.4 | 0.6 | 0.2 | 5.4 | 4.4 | 8.9 | 9.3 | 11.3 | 12.1 | 12.6 | 13.4 | 13.4 | 12.9 | 16.0 | 14.1 | 12.2 | 16.4 |
| $Fe_2O_3$ | 9.1 | 1.1 | 0.5 | 0.2 | 4.2 | 3.6 | 7.0 | 7.5 | 8.9 | 9.6 | 9.8 | 10.8 | 10.1 | 9.0 | 12.6 | 11.2 | 15.5 | 13.5 |
| MnO | 0.1 | 0.0 | 0.0 | 0.0 | 0.0 | 0.0 | 0.0 | 0.0 | 0.0 | 0.0 | 0.0 | 0.0 | 0.0 | 0.0 | 0.1 | 0.1 | 0.2 | 0.3 |
| MgO | 6.1 | 15.8 | 22.0 | 21.3 | 14.5 | 15.5 | 9.6 | 9.1 | 6.6 | 5.8 | 4.9 | 4.4 | 4.2 | 5.5 | 2.9 | 4.5 | 8.0 | 3.4 |
| CaO | 4.8 | 0.0 | 0.0 | 0.0 | 0.1 | 0.1 | 0.3 | 0.3 | 0.3 | 0.5 | 0.3 | 0.4 | 0.3 | 0.2 | 0.8 | 0.9 | 13.5 | 0.6 |
| $Na_2O$ | 1.7 | 0.0 | 0.0 | 0.0 | 0.1 | 0.1 | 0.3 | 0.3 | 0.4 | 0.4 | 0.5 | 0.4 | 0.7 | 0.4 | 0.8 | 0.6 | 1.7 | 0.8 |
| $K_2O$ | 2.4 | 0.2 | 0.1 | 0.0 | 0.9 | 0.6 | 1.5 | 1.5 | 1.8 | 2.0 | 2.0 | 2.1 | 2.4 | 1.8 | 2.4 | 1.9 | 0.9 | 2.9 |
| $P_2O_5$ | 0.6 | 0.0 | 0.0 | 0.0 | 0.0 | 0.0 | 0.1 | 0.1 | 0.1 | 0.1 | 0.1 | 0.2 | 0.1 | 0.1 | 0.3 | 0.3 | 1.2 | 0.1 |
| LOI | 8.3 | 17.7 | 17.6 | 17.8 | 17.4 | 18.1 | 15.2 | 15.3 | 15.3 | 13.8 | 14.1 | 14.6 | 13.6 | 15.3 | 11.7 | 13.7 | 2.4 | 6.6 |
| Li | 17.2 | 6.1 | 4.5 | 2.7 | 9.6 | 4.2 | 11.5 | 10.9 | 14.4 | 12.8 | 12.3 | 12.2 | 16.3 | 11.7 | 28.8 | 21.1 | 16.3 | 35.3 |
| Rb | 60 | 7 | 3 | 1 | 28 | 12 | 49 | 51 | 67 | 62 | 55 | 65 | 71 | 60 | 47 | 45 | 7 | 62 |
| Cs | 1.7 | 0.2 | 0.1 | 0.0 | 0.7 | 0.3 | 1.2 | 1.3 | 1.8 | 1.6 | 1.5 | 1.7 | 1.7 | 1.6 | 1.6 | 1.3 | 0.3 | 1.9 |
| Be | 1.8 | 0.1 | 0.1 | 0.0 | 0.6 | 0.2 | 0.9 | 0.9 | 1.6 | 1.2 | 1.1 | 1.3 | 1.4 | 1.2 | 1.8 | 1.6 | 1.5 | 2.7 |
| Sr | 558 | 62 | 26 | 52 | 84 | 36 | 71 | 69 | 80 | 74 | 64 | 75 | 212 | 63 | 227 | 186 | 982 | 229 |
| Ba | 708 | 1751 | 733 | 1500 | 1810 | 700 | 696 | 653 | 152 | 146 | 141 | 153 | 3027 | 132 | 1341 | 1611 | 591 | 237 |
| Sc | 17.5 | 1.7 | 1.1 | 0.6 | 6.8 | 2.7 | 11 | 11.3 | 14.2 | 12.8 | 12.9 | 14.8 | 14.1 | 13 | 11.1 | 14.5 | 23.7 | 14.9 |
| V | 170.0 | 49.3 | 37.0 | 31.1 | 207.4 | 85.2 | 366.9 | 344.1 | 423.6 | 435.1 | 459.6 | 542.7 | 422.9 | 377.0 | 661.5 | 440.8 | 413.2 | 530.8 |
| Cr | 335.8 | 20.8 | 22.3 | 11.7 | 111.4 | 62.7 | 184.5 | 218.4 | 239.6 | 267.5 | 284.4 | 304.6 | 249.6 | 186.9 | 287.6 | 219.5 | 555.2 | 300.0 |
| Co | 23.3 | 5.9 | 4.4 | 3.2 | 15.5 | 5.6 | 16.1 | 12.5 | 9.0 | 10.5 | 11.1 | 7.9 | 7.0 | 5.7 | 23.4 | 13.2 | 54.3 | 50.3 |
| Ni | 121.7 | 54.0 | 70.5 | 67.8 | 90.5 | 36.4 | 89.3 | 85.7 | 74.9 | 72.9 | 83.7 | 77.1 | 75.6 | 64.6 | 117.8 | 94.8 | 198.8 | 254.2 |
| Cu | 42.2 | 30.6 | 19.1 | 17.0 | 28.9 | 14.0 | 34.5 | 32.5 | 36.1 | 35.0 | 35.6 | 37.9 | 35.2 | 33.0 | 75.1 | 45.8 | 46.5 | 45.6 |
| Zn | 129.2 | 35.1 | 23.6 | 21.7 | 53.9 | 30.1 | 74.9 | 74.4 | 85.8 | 82.9 | 85 | 87.8 | 87.3 | 81.5 | 236.7 | 105.3 | 125.1 | 110.4 |
| Ga | 18.6 | 2.3 | 1.2 | 0.8 | 7.9 | 3.4 | 12.7 | 13.6 | 19.1 | 17.3 | 16.8 | 19.8 | 22.3 | 22.4 | 22.5 | 24.0 | 19.8 | 23.0 |
| Y | 29.2 | 1.0 | 0.4 | 0.2 | 4.9 | 2.1 | 7.1 | 7.9 | 8.3 | 8.4 | 8.1 | 10.2 | 11.2 | 7.2 | 8.9 | 15.6 | 30.7 | 27.1 |
| Nb | 68.7 | 7.0 | 2.4 | 0.9 | 22.5 | 10.2 | 38.5 | 40.8 | 56.3 | 52.2 | 50.1 | 55.3 | 60.7 | 51.0 | 80.9 | 68.8 | 68.9 | 75.4 |
| Ta | 4.5 | 0.5 | 0.2 | 0.1 | 1.4 | 0.7 | 2.3 | 2.4 | 3.3 | 3.1 | 2.9 | 3.2 | 3.5 | 2.9 | 4.5 | 3.8 | 4.5 | 4.8 |
| Zr | 451 | 57 | 23 | 12 | 187 | 168 | 310 | 322 | 379 | 390 | 436 | 406 | 484 | 438 | 509 | 500 | 308 | 438 |
| Hf | 7.1 | 0.7 | 0.3 | 0.1 | 2.5 | 1.0 | 4.2 | 4.4 | 5.7 | 5.3 | 5.0 | 5.8 | 6.3 | 5.3 | 7.7 | 6.7 | 8.0 | 10.1 |
| Mo | 6.0 | 0.5 | 0.5 | 229.3 | 106.7 | 73.3 | 14.6 | 40.9 | 129.8 | 27.4 | 43.9 | 66.0 | 130.1 | 85.0 | 124.4 | 27.2 | 2.6 | 2.9 |
| Sn | 0.2 | 0.0 | 0.0 | 0.0 | 0.1 | 0.1 | 0.2 | 0.2 | 0.3 | 0.2 | 0.2 | 0.2 | 0.3 | 0.2 | 0.2 | 0.2 | 0.0 | 0.3 |
| Tl | 12 | 1 | 0 | 0 | 2 | 1 | 5 | 5 | 7 | 6 | 5 | 7 | 6 | 5 | 15 | 6 | 3 | 10 |
| Pb | 1.68 | 0.12 | 0.06 | 0.03 | 0.61 | 0.28 | 1.00 | 1.15 | 1.94 | 1.65 | 1.39 | 1.62 | 1.85 | 1.54 | 2.15 | 2.17 | 1.75 | 5.03 |
| U | 8.1 | 0.6 | 0.2 | 0.1 | 2.9 | 1.1 | 4.7 | 4.8 | 5.9 | 4.9 | 5.3 | 5.9 | 5.9 | 4.0 | 3.9 | 5.6 | 6.3 | 10.1 |
| Th | 54.0 | 1.8 | 0.8 | 0.3 | 9.9 | 3.9 | 15.5 | 16.1 | 22.2 | 18.5 | 17.8 | 24.2 | 27.2 | 16.5 | 25.2 | 28.1 | 67.8 | 66.1 |
| La | 105.6 | 3.7 | 1.9 | 0.6 | 34.5 | 10.1 | 44.6 | 49.5 | 57.1 | 36.1 | 45.7 | 61.4 | 58.1 | 34.1 | 68.5 | 50.7 | 140.1 | 154.6 |
| Ce | 12.5 | 0.4 | 0.2 | 0.1 | 2.5 | 0.9 | 3.6 | 3.7 | 3.9 | 3.3 | 3.5 | 4.8 | 5.1 | 3.0 | 4.4 | 5.7 | 17.6 | 15.0 |
| Pr | 46.8 | 1.4 | 0.7 | 0.2 | 9.2 | 3.2 | 12.6 | 12.9 | 12.9 | 11.4 | 12.1 | 16.8 | 17.2 | 10.2 | 14.7 | 20.3 | 71.7 | 55.1 |
| Nd | 8.83 | 0.26 | 0.13 | 0.05 | 1.74 | 0.60 | 2.33 | 2.42 | 2.21 | 2.00 | 2.10 | 3.03 | 3.02 | 1.77 | 2.37 | 3.48 | 14.38 | 10.66 |
| Sm | 2.33 | 0.41 | 0.17 | 0.33 | 0.78 | 0.28 | 0.68 | 0.70 | 0.56 | 0.50 | 0.51 | 0.76 | 0.95 | 0.46 | 0.89 | 1.28 | 4.26 | 3.02 |
| Eu | 6.85 | 0.19 | 0.09 | 0.03 | 1.29 | 0.45 | 1.73 | 1.83 | 1.75 | 1.58 | 1.65 | 2.29 | 2.33 | 1.42 | 1.94 | 3.04 | 11.21 | 8.40 |
| Gd | 0.98 | 0.03 | 0.01 | 0.01 | 0.19 | 0.07 | 0.26 | 0.28 | 0.27 | 0.24 | 0.25 | 0.34 | 0.36 | 0.22 | 0.28 | 0.44 | 1.50 | 1.20 |
| Tb | 5.02 | 0.16 | 0.08 | 0.03 | 0.97 | 0.36 | 1.35 | 1.46 | 1.48 | 1.37 | 1.39 | 1.77 | 1.95 | 1.21 | 1.40 | 2.36 | 7.21 | 6.33 |
| Dy | 0.95 | 0.03 | 0.02 | 0.01 | 0.18 | 0.07 | 0.26 | 0.28 | 0.30 | 0.29 | 0.28 | 0.35 | 0.38 | 0.25 | 0.27 | 0.46 | 1.25 | 1.14 |
| Ho | 2.37 | 0.09 | 0.04 | 0.02 | 0.42 | 0.18 | 0.66 | 0.71 | 0.78 | 0.78 | 0.75 | 0.89 | 1.01 | 0.67 | 0.71 | 1.12 | 2.62 | 2.69 |
| Er | 0.37 | 0.01 | 0.01 | 0.00 | 0.07 | 0.03 | 0.11 | 0.12 | 0.13 | 0.13 | 0.13 | 0.15 | 0.17 | 0.11 | 0.11 | 0.17 | 0.35 | 0.39 |
| Tm | 2.15 | 0.09 | 0.04 | 0.02 | 0.39 | 0.19 | 0.63 | 0.69 | 0.81 | 0.78 | 0.76 | 0.90 | 1.01 | 0.67 | 0.64 | 0.99 | 1.86 | 2.19 |
| Yb | 0.30 | 0.01 | 0.01 | 0.00 | 0.06 | 0.03 | 0.09 | 0.10 | 0.12 | 0.12 | 0.11 | 0.13 | 0.15 | 0.10 | 0.10 | 0.14 | 0.27 | 0.33 |
| Lu | 17.20 | 6.10 | 4.50 | 2.70 | 9.60 | 4.20 | 11.50 | 10.90 | 14.40 | 12.80 | 12.30 | 12.20 | 16.30 | 11.70 | 28.80 | 21.10 | 16.30 | 51.85 |

in this area. If carbonates had precipitated and then dissolved by fluid flow focused on these areas it would be expected that the alteration of the tephra would be greater than in other areas where carbonates were not dissolved. Instead, tephra weathering is lower and very similar to that of a point at the same depth (280 cm) where carbonates precipitated, suggesting that the intensity of tephra alteration is controlled by some physical variable such as permeability, which was reduced at this depth in the entire horizon or in part of it. These considerations suggest that the absence of carbonates in the Bt lenses is not due to dissolution after precipitation. According to this, Bt lenses are produced by the alteration of deep tephra levels (within the Bkkm2 and Bkkm3 horizons) without carbonate precipitation. However, as indicated above, it is almost certain that the soil experienced several cycles or stages of carbonate precipitation perhaps including dissolution-reprecipitation due to variations of the hydrologic conditions, and the present carbonate distribution corresponds to the superposition of these cycles. In any case, the prevalence of palygorskite and sepiolite over smectite indicates that arid or semi-arid conditions were prevalent during soil formation.

## 6. Conclusions

The present investigation of clay minerals and carbonates in a soil developed on volcanic tephra is a remarkable example of how a combination of a particular texture with specific rock and fluid compositions generate a pattern of mineral distribution in a substrate of fairly homogeneous characteristics. Palygorskite and, in a lesser amount, smectite are generated within tephra grains, where Al and Fe, immobile elements, are available to be incorporated into the clay crystal structure. Sepiolite precipitates in the space between original tephra grains where Si and Mg, soluble and mobile elements, are abundant. The marked immobility of Al and Fe is probably exacerbated by the arid conditions in which the soils formed, which reduced the possibility that Al and Fe were transported either as dissolved species or as colloidal oxyhydroxide phases. Similar to sepiolite, calcite precipitated within the open space between tephra grains in the soil, whereas dolomite did only within volumes confined by the clay and tephra fabrics.

These results are relevant to the “dolomite problem” and shed light on the conditions in which dolomite can precipitate at surface

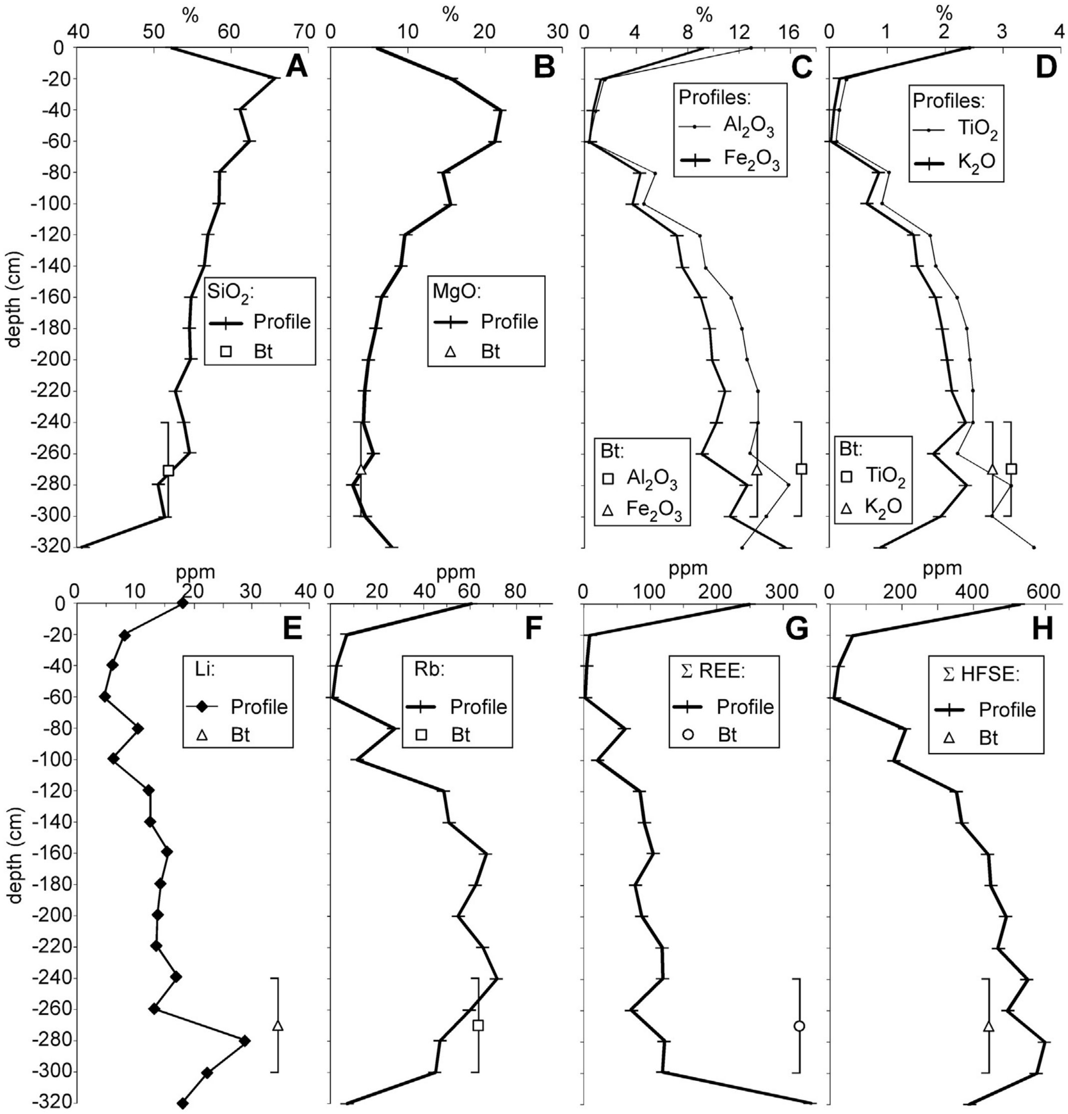

**Fig. 13.** Major (A–D) and trace element (E–F) distribution along the studied profile. Samples at 0 and 320 cm depth correspond to the reworked Ap horizon and the underlying basalt, respectively. Chemical composition for the studied sample (~270 cm depth) from the Bt level (240–300 cm depth) is indicated separately by different symbols.

environments. The results indicate that a viscous medium can overcome the kinetic advantage of calcite precipitation over dolomite. Perhaps, the initial precipitated phase in this environment was not yet crystalline dolomite but it evolved towards it. In geologic time scale, it is possible that mature dolomite catalyzes further dolomite growth from solution, perhaps reducing the need of a confined viscous environment.

Precipitation of dolomite in modern soils is relevant to $CO_2$ sequestration, as it increases the potential amounts that are being naturally sequestered and those that can be sequestered by human design. Dolomite solubility product at 25 °C is eight orders of magnitude lower than those of calcite and aragonite (Brownlow, 1996) and, on average, Mg and Ca contents are similar in silicate-rich soils and sediments (Brownlow, 1996). These two facts indicate that the potential of dolomite to capture $CO_2$ is twice that of calcite plus aragonite, and that dolomite is a more stable $CO_2$ sink. It would be of interest to investigate the global frequency of dolomite-precipitating soils in order to assess whether this is a quantitatively relevant phenomenon. Natural (soils, sediments) and artificial Mg- and Ca-rich systems can be engineered to increase their viscosity and favor the precipitation of dolomite over calcite.

## Acknowledgements

This work was supported by the P11-RNM-7067 project from the Junta de Andalucía (C.E.I.C.-S.G.U.I.T.) (P11-RNM-7067). A.S.N. acknowledges support from the human resources training programme “Salvador de Madariaga” (Ministerio de Educación, Cultura y Deporte, Spain). Support was also provided by The Natural History Museum hosting the visits of A.S.N. and J.L.D.H. We would like to thank A. González, M. Mª Abad, C. Hernández, M. A. Hidalgo and J. Montes (C.I.C. and Department of Mineralogy, University of Granada) for the guidance with the analytical electron studies and sample preparation. We also thank two anonymous reviewers for their thoughtful and thorough comments.

## References

Arvidson, R.S., Mackenzie, J.A., 1999. The dolomite problem: control of precipitation kinetics by temperature and saturation state. Am. J. Sci. 299, 257–288.

Balcells, R., Barrera, J.L., Gómez, J.A., Hernán, F., Schmincke, H.U., Merlos, A., Ruiz Garcia, M.T., Brändle, J.L., Vidal, J.R., 1992. Gran Canaria, hoja 21–21 y 21–22 del Mapa Geológico de España a escala 1:100.000, IGME, Ministero de Industria y Energía (Sheets 21–21 and 21–22 of the Geologic Map of Spain, scale 1:100,000. IGME. Ministry of Industry and Energy), Madrid.

Bence, A.E., Albee, A.L., 1968. Empirical correction factors for the electron microanalysis of silicate and oxides. J. Geol. 76, 382–403.

Birsoy, R., 2002. Formation of sepiolite–palygorskite and related minerals from solution. Clay Clay Miner. 50, 736–745.

Bontognali, T.R., Vasconcelos, C., Warthmann, R.J., Dupraz, C., Bernasconi, S.M., McKenzie, J.A., 2008. Microbes produce nanobacteria-like structures, avoiding entombment. Geology 36, 663–666.

Bontognali, T.R., Vasconcelos, C., Warthmann, R.J., Bernasconi, S.M., Dupraz, C., Strohmenger, C.J., McKenzie, J.A., 2010. Dolomite formation within microbialmats in the coastal sabkha of Abu Dhabi (United Arab Emirates). Sedimentology 57, 824–844.

Botha, G.A., Hughes, J.C., 1992. Pedogenic palygorskite and dolomite in a Late Neogene sedimentary succession, nothwestern Transvaal, South Africa. Geoderma 53, 139–154.

Brownlow, A.H., 1996. Geochemistry. second ed. Prentice Hall, New Jersey.

Capo, R.C., Whipkey, C.E., Blachère, J.R., Chadwick, O.A., 2000. Pedogenic origin of dolomite in a basaltic weathering profile, Kohala peninsula, Hawaii. Geology 28, 271–274.

Chamley, H., 1989. Clay Formation Through Weathering, in: Clay Sedimentology. Springer-Verlag, Berlin, pp. 21–52.

Corma, A., Mifsud, A., Sanz, E., 1987. Influence of the chemical composition and textural characteristics of palygorskite on the acid leaching of octahedral cations. Clay Miner. 22, 225–232.

Deelman, J.C., 2011. Low-Temperature Formation of Dolomite and Magnesite (version 2.3). Geology Series. Compact Disc Publication, Eindhoven, The Netherlands (http:/www.jcdeelman.demon.nl/dolomite/bookprospectus.html).

Diaz-Hernandez, J.L., Sanchez Navas, A., Reyes, E., 2013. Isotopic evidence for dolomite formation in soils. Chem. Geol. 347, 20–33.

Garcia-Casco, A., 2007. Magmatic paragonite in trondhjemites from the Sierra del Convento mélange, Cuba. Am. Mineral. 92, 1232–1237.

Garcia-Casco, A., Sanchez-Navas, A., Torres-Roldán, R.L., 1993. Disequilibrium decomposition and breakdown of muscovite in high P–T gneises, Betic alpine belt (southern Spain). Am. Mineral. 78, 158–177.

Gile, L.H., 1961. A classification of ca horizons in soils of a desert region, Doña Ana County, New Mexico. Soil Sci. Soc. Proc. 52–61.

Gile, L.H., Peterson, F.F., Grossman, R.B., 1966. Morphological and genetic sequences of carbonate accumulation in desert soils. Soil Sci. 1015, 347–360.

Guillou, H., Pérez-Torrado, F.J., Hansen-Machin, A.R., Carracedo, J.C., Gimeno, D., 2004. The Plio-Quaternary volcanic evolution of Gran Canaria based on new K–Ar ages and magnetostratigraphy. J. Volcanol. Geotherm. Res. 135, 221–246.

Henisch, H.K., 1989. Crystals in Gels and Liesegang Rings. Cambridge University Press, Cambridge.

Kato, T., 2005. New accurate Bence–Albee α-factors for oxides and silicates calculated from the PAP correction procedure. Geostand. Geoanal. Res. 29, 83–94.

Kelleher, I.J., Redfern, S.A.T., 2002. Hydrous calcium magnesium carbonate, a possible precursor to the formation of sedimentary dolomite. Mol. Simul. 28, 557–572.

Kohut, C., Dudas, M.J., Muehlenbachs, K., 1995. Authigenic dolomite in a saline soil in Alberta, Canada. Soil Sci. Soc. Am. J. 59, 1499–1504.

Lorimer, G.W., Cliff, G., 1976. Analytical electron microscopy of minerals. In: Wenk, H.R. (Ed.), Electron Microscopy in Mineralogy. Springer-Verlag, Berlin, pp. 506–519.

Lumsden, D.N., 1979. Discrepancy between thin section and X-ray estimates of dolomite in limestone. J. Sediment. Petrol. 49, 429–435.

Machel, H.G., 2004. Concepts and models of dolomitization: a critical reappraisal. Geol. Soc. Lond., Spec. Publ. 235, 7–63.

Martín-Ramos, J.D., Diaz-Hernandez, J.L., Cambeses, A., Scarrow, J.H., López-Galindo, A., 2012. Pathways for quantitative analysis by X-ray diffraction. In: Aydinalp, C. (Ed.), An Introduction to the Study of Mineralogy. InTech, Rijeka, Croatia, pp. 73–92.

McDougall, I., Schmincke, H.U., 1976. Geochronology of Gran Canaria, Canary Islands: age of shield building volcanism and other magmatic phases. Bull. Volcanol. 40, 57–77.

McKenzie, J.A., Vasconcelos, C., 2009. Dolomite mountains and the origin of the dolomite rock of which they mainly consist: historical developments and new perspectives. Sedimentology 56, 205–219.

Michalski, J.R., Cuadros, J., Niles, P.B., Parnell, J., Rogers, A.D., Wright, S.P., 2013. Groundwater activity on Mars and implications for a deep biosphere. Nat. Geosci. 6, 133–138.

Moreno, A., Nave, S., Kuhlmann, H., Canals, M., Targarona, J., Freudenthal, T., Abrantes, F., 2002. Productivity response in the North Canary Basin to climate changes during the last 250 000 yr: a multi-proxy approach. Earth Planet. Sci. Lett. 196, 147–159.

Neaman, A., Singer, A., 2004. The effects of palygorskite on chemical and physico-chemical properties of soils: a review. Geoderma 123, 297–303.

Niles, P.B., Catling, D.C., Berger, G., Chassefière, E., Ehlmann, B.L., Michalski, J.R., Morris, R., Ruff, S.W., Sutter, B., 2012. Geochemistry of carbonates on Mars: implications for climate history and nature of aqueous environments. Space Sci. Rev. http://dx.doi.org/10.1007/s11214-012-9940-y.

Oelkers, E.H., Gislason, S.R., Matter, J., 2008. Mineral carbonation of CO$_2$. Elements 4, 333–337.

Pérez-Torrado, F.J., 2000. Vulcanoestratigrafía del Grupo Roque Nublo, Gran Canaria, (Ph.D). ULPGC-Cabildo de Gran Canaria (459 pp.).

Pérez-Torrado, F.J., Carracedo, J.C., Mangas, J., 1995. Geochronology and stratigraphy of the Roque Nublo Cycle, Gran Canaria, Canary Islands. J. Geol. Soc. Lond. 152, 807–818.

Pérez-Torrado, F.J., Martí, J., Mangas, J., Day, S., 1997. Ignimbrites of the Roque Nublo group, Gran Canaria, Canary Islands. Bull. Volcanol. 58, 647–654.

Podwojewski, P., 1995. The occurrence and interpretation of carbonate and sulphate minerals in a sequence of vertisols in New Caledonia. Geoderma 65, 223–248.

Robins, C.R., Brock-Hon, A.L., Buck, B.J., 2012. Conceptual mineral genesis models for calcic pendants and petrocalcic horizons, Nevada. Soil Sci. Soc. Am. J. 76, 1887–1903.

Rodríguez, M., Neris, J., Tejedor, M., Jiménez, C., 2010. Soil temperature regimes from different latitudes on a subtropical island (Tenerife, Spain). Soil Sci. Soc. Am. J. 74, 1662–1669.

Rodríguez-Blanco, J.D., Shaw, S., Benning, L.G., 2015. A route for the direct crystallization of dolomite. Am. Mineral. 100, 1172–1181.

Rodríguez-González, A., Fernández-Turiel, J.L., Pérez-Torrado, F.J., Hansen, A., Aulinas, M., Carracedo, J.C., Gimeno, D., Guillou, H., Paris, R., Paterne, M., 2009. The Holocene volcanic history of Gran Canaria island: implications for volcanic hazards. J. Quat. Sci. 24, 697–709.

Rodríguez-González, A., Fernández-Turiel, J.L., Pérez-Torrado, F.J., Paris, R., Gimeno, D., Carracedo, J.C., Aulinas, M., 2012. Factors controlling the morphology of monogenetic basaltic volcanoes: the Holocene volcanism of Gran Canaria (Canary Islands, Spain). Geomorphology 136, 31–44.

Sanchez-Navas, A., Martín-Algarra, A., Rivadeneyra, M.A., Melchor, S., Martin-Ramos, J.D., 2009. Crystal-growth behavior in Ca–Mg carbonate bacterial spherulites. Cryst. Growth Des. 9, 2690–2699.

Sánchez-Román, M., Romanek, C.S., Fernández-Remolar, D.C., Sanchez-Navas, A., MacKenzie, J.A., Amils-Pibernat, R., Vasconcelos, C., 2011. Aerobic biomineralization of Mg-rich carbonates: implications for natural environments. Chem. Geol. 281, 143–150.

Schmidt, M., Xeflide, S., Botz, R., Mann, S., 2005. Oxygen isotope fractionation during synthesis of CaMg-carbonate and implications for sedimentary dolomite formation. Geochim. Cosmochim. Acta 69, 4665–4674.

Schoeneberger, P.J., Wysocki, D.A., Benham, E.C., Soil Survey Staff, 2012. Field Book for Describing and Sampling Soils, Version 3.0. Natural Resources Conservation Service, National Soil Survey Center, Lincoln, NE.

Shermann, D.G., Shultz, F., Always, F.J., 1962. Dolomitization of soils of the Red River Valley, Minnesota. Soil Sci. 94, 304–313.

Singer, A., 1977. Dissolution of two Australian palygorskites in dilute acid. Clay Clay Miner. 25, 126–130.

Singer, A., 2002. Palygorskite and sepiolite. In: Dixon, J.B., Schulze, D.G. (Eds.), Soil Mineralogy with Environmental ApplicationsSSSA Book Series vol. 7. Madison, Soil Science Society of America, pp. 555–583.

Singer, A., Norrish, K., 1974. Pedogenic palygorskite occurrences in Australia. Am. Mineral. 59, 508–517.

Sobecki, T.M., Karathanasis, A.D., 1987. Quantification and compositional characterization of pedogenic calcite and dolomite in calcic horizons of selected Aquolls. Soil Sci. Soc. Am. J. 51, 683–690.

Soil Survey Staff, 2014. Keys to Soil Taxonomy. 12th ed. U.S. Department of Agriculture - Natural Resources Conservation Service, Washington, DC.

St. Arnaud, R.J., 1979. Nature and distribution of secondary soil carbonates within landscapes in relation to soluble Mg$^{2+}$/Ca$^{2+}$ ratios. Can. J. Soil Sci. 59, 87–98.

Thorseth, I.H., Fumes, H., Heldal, M., 1992. The importance of microbiological activity in the alteration of natural basaltic glass. Geochim. Cosmochim. Acta 56, 845–850.

Torres-Roldan, R., Garcia-Casco, A., 2003. DWImager: Una Implementación para el Procesamiento de Matrices de Intensidades de Rayos X. Unpublished report, Department of Mineralogy and Petrology, University of Granada.

Van Tuyl, F.M., 1916. The present status of the dolomite problem. Science 44, 688–690.

Vasconcelos, C., McKenzie, J.A., 1997. Microbial mediation of modern dolomite precipitation and diagenesis under anoxic conditions (Lagoa Vermelha, Rio de Janeiro, Brazil). J. Sediment. Petrol. 67, 378–390.

Vasconcelos, C., McKenzie, J.A., Bernasconi, S., Grujic, D., Tien, A.J., 1995. Microbial mediation as a possible mechanism for natural dolomite formation at low temperatures. Nature 377, 220–222.